ETC: TRAINING-FREE DIFFUSION MODELS ACCELERATION WITH ERROR-AWARE TREND CONSISTENCY

Anonymous authors
Paper under double-blind review

ABSTRACT

Diffusion models have achieved remarkable generative quality but remain bottlenecked by costly iterative sampling. Recent training-free methods accelerate diffusion process by reusing model outputs. However, these methods ignore denoising trends and lack error control for model-specific tolerance, leading to trajectory deviations under multi-step reuse and exacerbating inconsistencies in the generated results. To address these issues, we introduce Error-aware Trend Consistency (ETC), a framework that (1) introduces a consistent trend predictor that leverages the smooth continuity of diffusion trajectories, projecting historical denoising patterns into stable future directions and progressively distributing them across multiple approximation steps to achieve acceleration without deviating; (2) proposes a model-specific error tolerance search mechanism that derives corrective thresholds by identifying transition points from volatile semantic planning to stable quality refinement. Experiments show that ETC achieves a 2.65× acceleration over FLUX with negligible (-0.074 SSIM score) degradation of consistency.[1].

1 INTRODUCTION

Diffusion models (Sohl-Dickstein et al., 2015; Song & Ermon, 2019; Ho et al., 2020) have demonstrated remarkable generative capabilities across diverse domains including images, videos and audio. However, their superior generative performance typically requires larger model architectures and multi-step denoising processes, resulting in substantial computational overhead and inference latency. Training-based methods (Salimans & Ho, 2022; Luo et al., 2023) accelerate diffusion by learning a few-step model from the denoising process of a multi-step model. However, this paradigm requires extensive training and there often remains a discrepancy between the predictive distributions of the original and the few-step model (Stanton et al., 2021), weakening generalization capabilities.

In contrast, training-free methods (Chen et al.; Ye et al., 2024) accelerate diffusion without model retraining or performance degradation by leveraging feature similarity between adjacent timesteps, broadly categorized into inner-level and step-wise feature reuse mechanisms. Inner-level (Ma et al., 2024a; Liu et al., 2025b) methods accelerate inference by reusing internal layer features within each denoising iteration but require architecture-specific designs. In contrast, step-wise (Ye et al., 2024; Liu et al., 2025a) methods evaluate model output robustness to determine multi-step reuse and reduce the total number of model inferences, achieving better generalized acceleration compared to inner-level alternatives. However, step-wise methods overlook denoising trends between adjacent timesteps, leading to inconsistent generation results. While recent approaches (Chen et al.; Liu et al., 2025a) attempt to address this by employing residuals between model outputs for trend prediction, short-term output fluctuations often deviate from the long-term denoising trajectory, thereby exacerbating trend inconsistency caused by the multi-step use of fluctuating residuals as shown in Figure 1a. Consequently, achieving **multi-step approximations with consistent trajectories** remains an unresolved challenge. Moreover, existing methods rely on manually-defined fixed thresholds for approximation error assessment, neglecting model-specific error tolerances shown in Figure 1b. Consequently, fixed threshold strategy may fails to address scenarios where accumulated errors cause irreversible trajectory deviations beyond the model's corrective capacity, resulting in **inadequate error control** and amplified generation inconsistency. To summarize, step-wise feature

[1]More samples and source code are available at `https://etcdiff.github.io/`

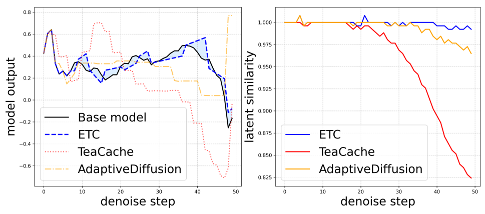

(a) Comparison of denoising trajectories

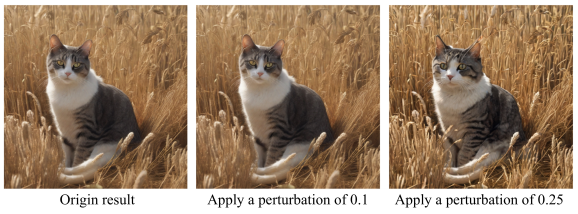

(b) Effect of different levels of denoising errors

Figure 1: Visualization of trajectory deviation and denoise error tolerance. Subfigure (a) shows that existing methods fail to follow the original denoising trajectory and reduce latent similarity. Subfigure (b) shows the model maintains consistent results to a certain degree of denoising errors.

reuse research demonstrates significant untapped acceleration potential but is challenged with trajectory deviations under multi-step approximation due to the lack of accurate capture of denoising trends, and inadequate error control due to insufficient exploration of model error tolerance limits.

To address the above problems, we propose ETC, a framework that achieves step-wise diffusion acceleration through trajectory consistency and model-specific error control. For the multi-step trajectory consistency problem, we aim to derive future directional flows from the global stabilization properties inherent in the denoising process. Specifically, we compute weighted projections of cross-step changes in model outputs, attenuating fluctuations caused by approximation errors while amplifying directional components of long-term dynamics. To further enhance acceleration, we design an adaptive expansion strategy that dynamically extends or contracts the approximation window based on whether deviations between projected trends and periodic model inferences remain within the model's corrective capacity. Moreover, we employ a progressive distribution paradigm that proportionally allocates estimated direction flows across each approximation step, thereby achieving aggressive acceleration while preventing divergence from the denoising trajectory. As for the inadequate error control problem, we treat different models' error tolerance as emergent properties within denoising dynamics. Observing that the semantic planning phase in denoising process exhibit high dynamic variance (Liu et al., 2025b), we quantify the perceptual influence of deviation perturbations on generation quality and derive critical transition points from volatile semantic planning to smooth quality refinement phases that reflect model limits for error correction.

In summary, the main contributions of out work are as follows: (1) We introduce a consistent trend predictor that projects stabilizing denoising trends into future flows and progressively distributes them across approximation steps to ensure trajectory consistency. (2) We propose a model-specific error tolerance search method that quantifies the impact of accumulated errors and locates the transition point between volatile semantic planning and stable quality refinement to reflect the error tolerance threshold. (3) Experiments show that ETC outperforms other state-of-the-art baselines in terms of generation consistency and speed across images, videos and audio synthesis.

2 RELATED WORK

Diffusion model Diffusion models have achieved great success in generative tasks. Early diffusion models (Ho et al., 2020; Song et al., 2020a) implemented iterative denoising processes directly on the original data modality, which imposed computational overhead due to high-dimensional operations. To address computational efficiency constraints, latent diffusion models (Rombach et al., 2022; Blattmann et al., 2023) compress the original modality into lower-dimensional representations before applying the diffusion process. Initially developed with the U-Net (Ronneberger et al., 2015), latent diffusion models have demonstrated impressive performance. However, U-Net-based design encountered scalability constraints that limited larger model training and practical deployment. Diffusion Transformers (DiT) (Peebles & Xie, 2023) address this limitation by leveraging transformer (Vaswani et al., 2017) for enhanced scalability and achieve state of-the-art performance across diverse domains (Labs, 2024; Wan et al., 2025; Hung et al., 2024). Despite the high quality achieved by diffusion models, the multi-step denoising design slows down the inference process.

Diffusion model acceleration Diffusion model acceleration can be categorized into training-based and training-free approaches. Training-based methods aim to learn a few-step model from the multi-step denoising process. Progressive distillation (Salimans & Ho, 2022) progressively matches

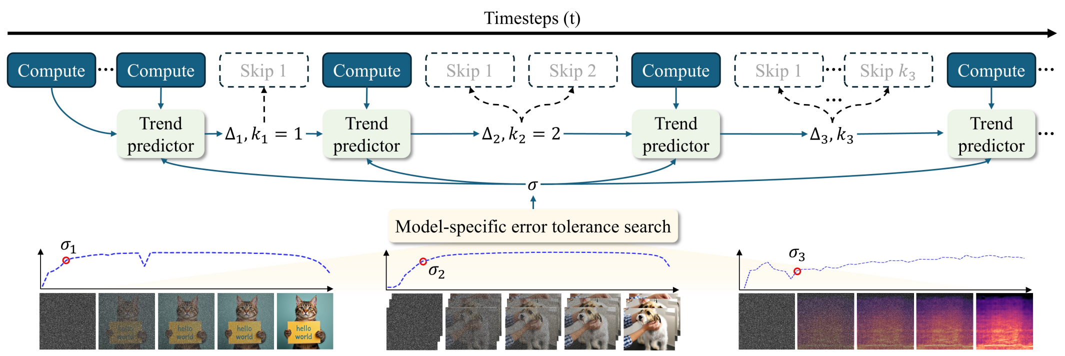

Figure 2: An overview of ETC. ETC leverages all historical model outputs to estimate future trends and dynamically adjusts approximation frequency according to each model's error tolerance limit.

noise predictions between teacher and student models. Latent Consistency Model (LCM) (Luo et al., 2023) achieves single-step sampling by imposing self-consistency constraints. However, these methods require time-consuming training and often suffer performance degradation due to the gap between the predictive distributions of the few-step and original models (Stanton et al., 2021).

In contrast, recent training-free approaches leverage feature reuse between adjacent time steps for acceleration and can be divided into inner-level and step-wise feature reuse. Inner-level reuse accelerates diffusion by reusing features within different layers of the model. DeepCache (Ma et al., 2024b) caches high-level features in the U-Net while dynamically updating only shallow features in subsequent steps. T-Gate (Liu et al., 2025b) caches DiT cross-attention outputs after convergence and keeps them fixed for remaining steps. However, these methods are model-specifically designed and lack generalizability. Step-wise methods exploit cross-temporal output similarity for general acceleration. AdaptiveDiffusion (Ye et al., 2024) detects redundancy across denoising steps using a third-order differential estimator and reuses historical model outputs. However, it neglects the denoising trend and leads to gradual trajectory deviations. TeaCache (Liu et al., 2025a) minimizes trajectory deviation by using residuals between adjacent steps as approximate trends, but it may amplify error accumulation due to short-term denoising fluctuations. SADA (Jiang et al., 2025) enhances trend estimation by combining three-step historical results, yet its acceleration potential is limited by a maximum four-step jump. Although step-wise methods show acceleration potential, maintaining trend consistency in multi-step approximations remains a challenge. Furthermore, existing step-wise methods rely on manually predefined thresholds to determine the reusability, resulting in inconsistent performance across different models due to the lack of model-specific thresholds.

In this paper, we focus on maintaining the consistency of denoised trajectories during step-wise acceleration. We combine all historical trend patterns to obtain more stable future direction estimates and identify model-specific error tolerances, ensuring the approximation process stays aligned with the original trajectory without significant deviation.

3 Methodology

In this section, we provide a detailed description of the architectural components of our proposed framework, ETC. As shown in Figure 2, the overall framework consists of two main modules: 1) Consistent trend predictor for predicting future denoising trends and approximate frequencies; 2) Model-specific error tolerance mechanism for identifying error thresholds across different models. The following subsections detail the design of each module.

3.1 Preliminary

Diffusion denoising process Diffusion models consist of a forward process that progressively corrupts data with Gaussian noise and a reverse process that reconstructs the clean data through iterative denoising. During inference, only the reverse process is executed, starting from the Gaussian noise $x_T \sim \mathcal{N}(0, I)$ and progressively refines x_T into the target output x_0 conditioned on input signal c (e.g., text prompts), where T is the predefined number of denoising steps. The refinement follows a

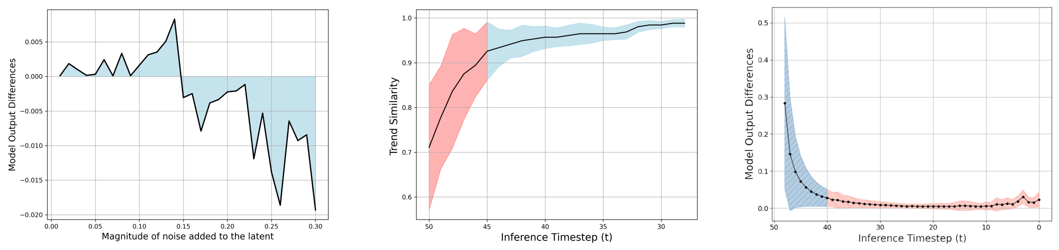

(a) Error correction (b) Similarity to historical trends (c) Two stages in denoising

Figure 3: The patterns of the denoising process observed during inference with FLUX on MSCOCO-2017 validation set. Subfigure (a) shows how the model output varies under different latent error. Subfigure (b) illustrates the similarity of current trend to each historical trends. Subfigure (c) depicts the stability of trend changes across different denoising stages.

generic update rule defined at each timestep t :

$$x_{t-1} = f(t-1) \cdot x_t - g(t-1) \cdot \epsilon_\theta(x_t, t, c), \quad t = 1, \dots, T, \tag{1}$$

where $\epsilon_\theta(x_t, t, c)$ is a noise prediction network trained to estimate the noise component in x_t by taking x_t, timestep t and an additional condition c as input, while $f(t)$ and $g(t)$ are coefficients determined by the sampler (a.k.a, scheduler) (Ho et al., 2020; Song et al., 2020a). Both the noise prediction network ϵ_θ and sampler coefficients $f(t)$, $g(t)$ directly impact generation quality. Using the same sampler ensures the consistency of $f(t)$ and $g(t)$, so the generation quality is primarily affected by the differences of the noise prediction model ϵ_θ. Detailed discussion is provided in Appendix A.2.

Fluctuation and stabilization phases of model outputs Previous works (Ho et al., 2020; Wu et al., 2024; Lee et al., 2025) have observed that diffusion models demonstrate substantial low-frequency changes in the early denoising steps, followed by more stable high-frequency refinements in later steps. Furthermore, Liu et al. (2025b) divided the denoising process into semantic planning phase and fidelity refinement phase by observing that cross-attention maps fluctuate in the early stage and become stable afterward. In alignment with these findings, we observe a similar pattern shown in Figure 3c by analyzing the difference in model outputs between two consecutive steps. Throughout most of the denoising process, model outputs between adjacent timesteps display stable change patterns. Therefore, we make the following assumption.

Assumption 1 The model output $\epsilon_\theta(x_t, t, c)$ is jointly Lipschitz continuous in both x_t and t, exhibiting structured and predictable variations across time steps.

The proof of Lipschitz continuity and a more detailed discussion of model output trends are provided in the Appendix A.2 and A.4. In this paper, we aim to estimate model outputs based on historical trends while ensuring cumulative errors do not cause significant deviations in the generated results.

3.2 CONSISTENT TREND PREDICTOR

Historical denoising pattern projections Based on Assumption 1, we can approximate the future denoised trajectory using the recent trend. However, as illustrated in Figure 3a, when the approximated trend introduces errors in the latent space, the model output increases compared to the original result in order to correct the cumulative error. Continuing to use this trend for future trajectory approximations leads to fluctuations and further exacerbates trajectory deviation. Therefore, our goal is to approximate trajectories by combining multiple historical trends, thereby minimizing the fluctuations introduced by the error-corrected model output.

Let $d_t^{t+1} = \epsilon_\theta(x_t, t, c) - \epsilon_\theta(x_{t+1}, t+1, c)$ represent the model outputs difference between time steps t and $t+1$. As shown in Figure 3b, recent historical trends more accurately reflect future changes, while even trends from earlier time steps maintain a similarity above 0.7, indicating they still capture some directional information. Therefore, we use a weighted sum of all historical trends, assigning higher weights to more recent trends. However, storing all historical trends incurs considerable computational overhead. To address this, we propose a recursive historical trend weighting method, formulated as follows:

$$\Delta_{t-2} = (1-\alpha)\Delta_{t-1} + \alpha d^{t}_{t-1}, 0 \leq t < T, \Delta_{T-2} = d^{T}_{T-1}, \tag{2}$$

where Δ_{t-2} represents the estimated trend starting from time step $t-2$, α is the trend adjustment coefficient used to reduce volatility caused by error correction while preserving consistency with the historical denoised trajectory. Only the model outputs and the final approximation value from each round of multi-step approximation are used to calculate the future estimated trends. Furthermore, as shown in Figure 3b, the correlation between the trend in the initial denoising stage and the future trend shows substantial fluctuations (the red area represents the variance). Therefore, we first allow the model to perform n denoising steps to obtain a more stable trend estimate before initiating the approximation. Once the estimated trend is obtained, we can calculate the approximation output $\epsilon_{\theta}^{'}$ using the following formula:

$$\epsilon_{\theta}^{'}(x_{t-2}, t-2, c) = \epsilon_{\theta}(x_{t-1}, t-1, c) + \Delta_{t-2} \tag{3}$$

Dynamic approximation window expansion strategy To achieve faster acceleration, our goal is to maximize the approximation frequency while maintaining trajectory consistency. We add a fixed value from the latent to represent the approximation error. As shown in Figure 3a, within the error correction range, the model can produce larger outputs to compensate for the reduced denoising caused by the error. However, if the error exceeds this range, the model's output begins to diverge from the original result. Based on this observation, we propose an approximation window expansion strategy. If the cumulative error of the previous iteration is below the threshold, the approximation step for the next iteration increases; otherwise, it decreases. The formula is as follows:

$$k_{t-2} = \begin{cases} k_{t-1}+1, & |d^{t}_{t-1} - \Delta_{t-1}| < \psi, \\ k_{t-1}-1, & |d^{t}_{t-1} - \Delta_{t-1}| \geq \psi, \end{cases} \tag{4}$$

where k is the approximation step and ψ is the threshold. To maintain consistency in multi-step approximations, we distribute the estimated trend averagely across each step. This design ensures that the final approximation direction aligns with the estimated trend, preventing the accumulation of estimation errors that could lead to trajectory deviation. The formula for calculating the approximation output at each step is as follows:

$$\epsilon_{\theta}^{'}(x_{t-1-s,t-1-s,c}) = \epsilon_{\theta}(x_t - 1, t-1, c) + \frac{s}{k_{t-2}}\Delta_{t-2}, 1 \leq s \leq k_{t-2}. \tag{5}$$

Error estimation The detailed analysis of estimation errors is provided in Appendix A.1. Assuming $\alpha = 0.5$, the formulation for the upper bound of cumulative error is as follows:

$$error_r \leq \| \sum_{m=0}^{k_r-1} ((1+\frac{k_r-m}{2k_r})\sigma_{r-1} + \frac{k_r-m}{2k_r} \cdot d^{T-n-\sum_{l=1}^{r-2}(k_l+1)}_{T-n-\sum_{l=1}^{r-1}(k_l+1)} - d^{T-n-\sum_{j=1}^{m-1}(k_j+1)}_{T-n-\sum_{j=1}^{m}(k_j+1)-k_r+m})\|. \tag{6}$$

Let $t = T - n - \sum_{l=1}^{r-2}(k_l+1)$. As shown in Figure 4, the approximation error depends on the alignment between the approximated trend (a weighted combination of d and σ) and the future trend. Assuming $\sigma = 0$, the error depends solely on how much the future trend deviates from that of the previous round, ensuring that the denoised trajectory remains at least consistent with the prior step. Consequently, as long as the cumulative error in the early rounds is limited and σ remains small, the estimated trend remains controllable and the denoising trajectory maintains consistency.

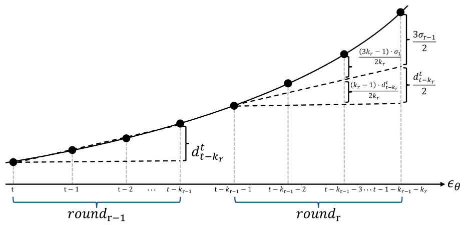
$\frac{3\sigma_{r-1}}{2}$
$\frac{(3k_r-1)\cdot\sigma_1}{2k_r}$
$\frac{d^t_{t-k_r}}{2}$
$\frac{(k_r-1)\cdot d^t_{t-k_r}}{2k_r}$
$d^t_{t-k_r}$
ϵ_θ
t
$t-1$
$t-2$
$\cdots$
$t-k_{r-1}$
$t-k_{r-1}-1$
$t-k_{r-1}-2$
$t-k_{r-1}-3 \cdots t-1-k_{r-1}-k_r$
$round_{r-1}$
$round_r$

Figure 4: Error accumulation at $\alpha = 0.5$.

3.3 Model-specific error tolerance search mechanism

Necessity of error control Assuming that a fixed error β is introduced at every timestep, the accumulated error at the final timestep can be formulated as:

$$error = \sum_{m=0}^{T-2}\left(\left(\prod_{j=0}^{T-2-m} f(j)\right) \cdot g(T-1-m) \cdot \beta\right) + g(0) \cdot \beta. \tag{7}$$

The proof can be found in Appendix A.5. As shown in Equation 7, any error introduced during the denoising process will progressively accumulate and be amplified. Therefore, it is necessary to ensure the accumulated error within a single approximation round does not lead to trajectory deviation. Otherwise, the deviation will be further amplified over multiple rounds, degrading the final generation quality.

Error tolerance search When model outputs exhibit semantic planning volatility, trajectory deviation may occurs and subsequent steps amplify errors. Therefore, we regard the semantic planning phase as fluctuations that occur outside the model's error tolerance range. By identifying the transition point from this fluctuating phase to the stable quality enhancement phase, we can approximate the model's error tolerance limit. Specifically, we introduce the model output difference d from each denoising step as as an accumulated error added to the final latent and compute the similarity between the perturbed result and the original generated result:

$$s_i = Sim(D(x_0 + d_i), D(x_0)), \quad i = 1, ..., T, \tag{8}$$

where x_0 is the denoised output at the final timestep, D is the decoder and Sim is the similarity metrics. Using trend inflection point analysis tools (e.g., the ruptures package) to analyze the similarity trend, we can determine the model output difference at the transition point between the two phases, which corresponds to our estimated model error tolerance limit. The detailed process of error tolerance search and inflection point analysis is provided in Appendix A.7 and A.11.

4 EXPERIMENTS

4.1 EXPERIMENTAL SETTINGS

Base models and compared methods To demonstrate the general effectiveness of our method, we apply our technique to various diffusion models for image, video, and audio generation, including SDXL (Podell et al., 2023) and Flux (Labs, 2024) for image, Open-Sora 1.2 (Zheng et al., 2024) and Wan 2.1 (Wan et al., 2025) for video, and TangoFlux (Hung et al., 2024) for audio. We compare our method with recent state-of-the-art acceleration approaches, including AdaptiveDiffusion (Ye et al., 2024), SADA (Jiang et al., 2025), TeaCache (Liu et al., 2025a) and MagCache (Ma et al., 2025). To better assess the efficiency-quality trade-off, we utilize the fast configurations of TeaCache and MagCache for fair comparison.

Evaluation metrics and datasets We evaluate acceleration methods across two key dimensions: computational efficiency and generation quality. For efficiency assessment, we report Floating Point Operations (FLOPs), inference latency and speedup ratios. For quality evaluation, we employ modality-specific metrics to comprehensively assess the fidelity between accelerated and original outputs. For image and video generation, we measure visual similarity using LPIPS (Zhang et al., 2018), PSNR, and SSIM. Additionally, we evaluate text-image alignment using CLIP score (Radford et al., 2021) for images and employ VBench (Huang et al., 2024) for multi-aspect video quality assessment. For audio generation, we measure acoustic fidelity using FAD (Kilgour et al., 2018), MCD (Kubichek, 1993), and KL-divergence of classification probabilities (Copet et al., 2023; Koutini et al., 2021), while assessing text-audio alignment with CLAP score (Wu et al., 2023). To ensure fair comparison, all experiments are conducted using standardized prompt datasets: MSCOCO-2017 (Lin et al., 2014) validation set for image generation, VBench prompts for video generation and AudioCaps (Kim et al., 2019) test set for audio generation.

Implementation details All experiments are conducted on a same GPU using PyTorch, with FlashAttention (Dao et al., 2022) enabled across all configurations. To efficiently determine the step-skipping threshold, we sample a small set of prompts for each modality. For image and audio models, we partition MSCOCO-2017 and AudioCaps training prompts into 10 length-based bins and sample one prompt per bin. For video models, we sample one prompt from each VBench evaluation dimension. Threshold results are provided in Table 1. The hyperparameter n is set to 4 for OpenSora and 6 for the remaining models, while α is all set to 0.5. SDXL, FLUX, OpenSora and TangoFlux use the Euler solver, while Wan uses the UniPC solver (Zhao et al., 2023).

4.2 MAIN RESULTS

Quantitative comparison Table 1 presents quantitative results evaluating both computational efficiency and generation quality. ETC achieves superior acceleration performance across diverse tasks

Table 1: Quantitative evaluation results. Best performance in **bold**, and the second best underlined. Our method achieves superior efficiency-quality trade-off across diverse tasks and architectures.

Method	Visual Quality				Efficiency		
Text to Image	**LPIPS ↓**	**SSIM ↑**	**PSNR ↑**	**CLIP ↑**	**FLOPs (P) ↓**	**Speedup ↑**	**Latency (s) ↓**
SDXL ($T = 50$)	-	-	-	27.253	0.67	1×	9.63
AdaptiveDiffusion	0.172	0.816	25.062	27.048	0.31	1.98×	4.87
SADA	**0.096**	**0.882**	**28.881**	27.055	0.35	1.81×	5.07
Ours ($\sigma = 0.0171$)	0.105	0.876	28.017	**27.103**	**0.26**	**2.12×**	**4.53**
FLUX ($T = 50$)	-	-	-	26.319	3.64	1×	28.85
TeaCache-fast	0.281	0.753	18.845	25.924	1.45	2.45×	11.78
SADA	**0.062**	0.923	**29.342**	25.979	1.74	2.07×	13.94
Ours ($\sigma = 0.1269$)	0.068	**0.926**	29.176	**25.983**	**1.31**	**2.65×**	**10.86**
Text to Video	**LPIPS ↓**	**SSIM ↑**	**PSNR ↑**	**VBench ↑**	**FLOPs (P) ↓**	**Speedup ↑**	**Latency (s) ↓**
Open-Sora 1.2 ($T = 30$)	-	-	-	77.18%	3.15	1×	45.29
TeaCache-fast	0.217	0.775	20.601	76.10%	1.51	2.06×	21.95
MagCache-fast	0.164	0.823	22.583	75.84%	1.41	2.11×	21.45
Ours ($\sigma = 0.2101$)	**0.131**	**0.848**	**24.123**	**76.44%**	**1.32**	**2.15×**	**21.07**
Wan 2.1 ($T = 50$)	-	-	-	81.01%	76.71	1×	970.49
TeaCache-fast	0.317	0.587	17.329	80.06%	38.63	1.91×	508.31
MagCache-fast	0.135	0.787	22.867	80.63%	32.49	2.38×	407.64
Ours ($\sigma = 0.1181$)	**0.103**	**0.806**	**24.078**	**80.71%**	**28.63**	**2.49×**	**389.89**
Text to Audio	**FAD ↓**	**MCD ↓**	**KL ↓**	**CLAP ↑**	**FLOPs (T) ↓**	**Speedup ↑**	**Latency (s) ↓**
TangoFlux ($T = 50$)	-	-	-	13.286	46.86	1×	5.49
TeaCache-fast	0.101	3.598	0.187	13.225	16.58	2.27×	2.42
AdaptiveDiffusion	0.042	3.145	0.181	**13.309**	27.91	1.48×	3.72
Ours ($\sigma = 0.0675$)	**0.026**	**1.877**	**0.157**	13.251	**14.83**	**2.43×**	**2.26**

and architectures while maintaining high visual quality. In evaluating the Wan 2.1 text-to-video baseline, our method achieves a 2.5× speedup while maintaining the highest SSIM of 0.806, outperforming MagCache which attains only 2.38× acceleration with 5% lower generation consistency. With the TangoFlux text-to-audio baseline, our approach delivers the highest speedup of 2.43× with an MCD score 40% lower than AdaptiveDiff, which achieves only 1.48× acceleration due to its design prioritizing generation quality. For text-to-image baselines, our method achieves a 2.65× speedup on Flux with an SSIM of 0.926. Although our SSIM on SDXL is 0.6% lower than SADA, we achieve 22% faster inference, demonstrating a superior efficiency-quality trade-off.

Visualization Figure 5 compares the results generated by ETC against those by the original model and other baselines. For image generation, TeaCache and AdaptiveDiff exhibit noticeable structural distortions, such as changes in car front designs and chair leg deformations. Although SADA preserves the overall structure, it suffers from detail loss and text generation errors, such as the extra piece of litter near the chair and the altered license plate from ”NX4 5KJ” to ”AX4 5K”. For video generation, TeaCache shows significant content deviation, with differences in dog appearance and petting gestures. MagCache maintains structural alignment but loses fine details such as raccoon fur texture and the distinctive yellow whiskers around the dog's mouth. For audio generation, while the task complexity is relatively lower and most methods preserve similarity to original results, TeaCache still introduces artifacts such as noise distortions highlighted in the red box. In contrast, our method preserves both global consistency and fine-grained detail through various tasks, demonstrating superior generation fidelity.

4.3 Ablation Studies

Statistical robustness To evaluate the stability of generation performance across diverse text conditions, we analyze the distribution of SSIM and latency metrics using box plots for all three generation tasks. As shown in Figure 6, TeaCache and MagCache exhibit stable acceleration performance with narrow latency distributions across different prompts. However, for Wan 2.1, TeaCache's SSIM spans a wide range from 0.1 to 0.9, while MagCache shows slight improvement but still ranges from 0.5 to 0.9. In contrast, our method shows moderate latency variance but achieves significantly tighter SSIM distributions of 0.7 to 0.9. While SADA and AdaptiveDiff show similar adaptive behavior with moderate latency variation, both methods suffer from quality instability with numerous outliers compared to our method. These results demonstrate that ETC effectively balances acceleration and stability, achieving more consistent generation quality across diverse conditions.

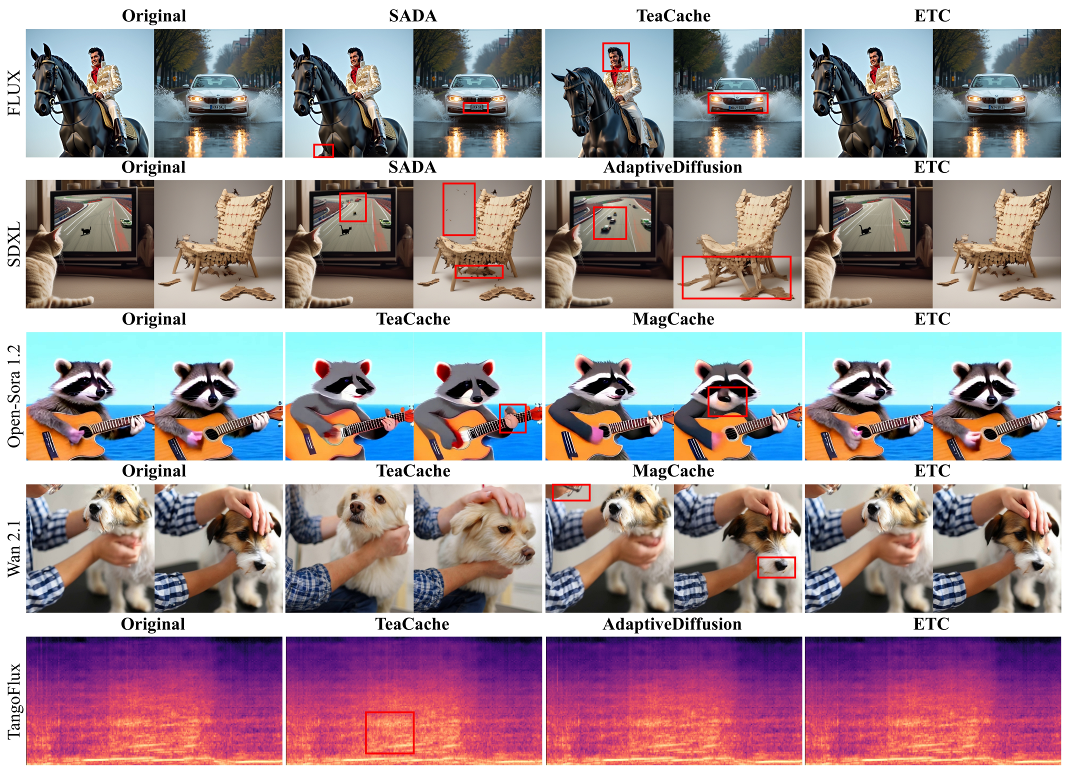

Figure 5: Comparison of visual quality with the competing method. Other methods exhibit issues such as text failure and missing details, whereas ETC achieves the best generation consistency.

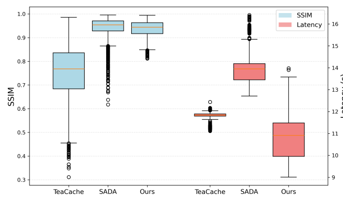

(a) FLUX

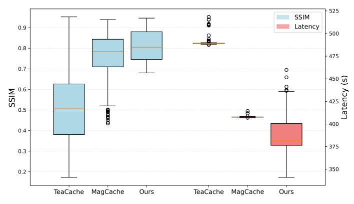

(b) Wan 2.1

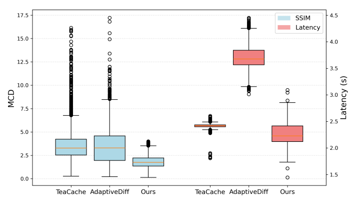

(c) TangoFlux

Figure 6: Boxplots of SSIM and latency metrics across different tasks.

Effectiveness of error control To investigate error accumulation from approximate noise, we computed differences between approximated and actual noise at each timestep, along with corresponding latent bias. As shown in Figure 7, noise error exhibits two distinct patterns: fluctuating increase and steady increase. TeaCache demonstrates steady error growth due to its simplistic approximation using adjacent historical noise differences, introducing significant bias during high-fluctuation initial phases that propagates throughout denoising. Our method follows the fluctuating pattern but accumulates error slower than MagCache and AdaptiveDiff. While SADA exhibits a similar error accumulation pattern to ours, it achieves lower accumulation rates by sacrificing inference speed. In contrsast, our approach maintains high acceleration while effectively controlling error accumulation, demonstrating that our trend approximation strategy preserves denoising trajectory consistency during multiple approximations.

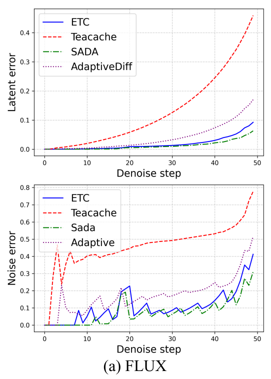

(a) FLUX

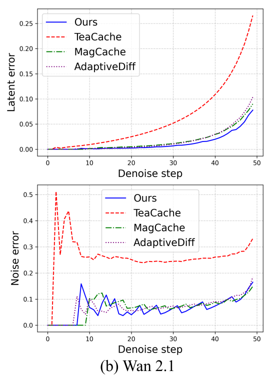

(b) Wan 2.1

Figure 7: Accumulation of denoising errors.

Table 2: Variation in speed and generation quality under different expansion threshold settings.

FLUX	σ	0.4429	0.2435	0.2263	0.1921	0.1269	0.1027	0.0798	0.0597	0.0392
	Latency (s) ↓	8.64	9.06	9.61	9.62	10.86	11.37	11.95	13.69	14.66
	SSIM ↑	0.823	0.851	0.887	0.893	0.926	0.927	0.942	0.965	0.980
	CLIP ↑	25.679	25.437	25.817	25.769	25.983	26.281	26.169	26.323	26.494
Wan 2.1	σ	0.4225	0.2762	0.2102	0.1523	0.1181	0.0869	0.0761	0.0678	0.0487
	Latency (s) ↓	293.76	293.78	342.91	369.97	389.89	496.15	505.88	536.82	538.68
	SSIM ↑	0.637	0.637	0.708	0.762	0.806	0.821	0.843	0.889	0.912
	VBench ↑	80.61%	80.61%	80.25%	80.56%	80.71%	80.72%	80.78%	80.95%	81.10%

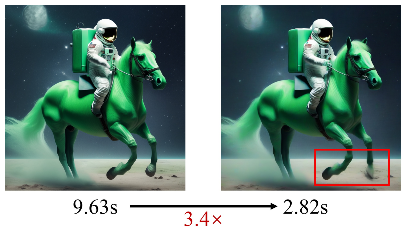

(a) SDXL

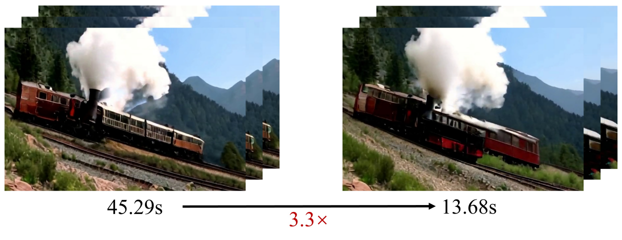

(b) Open-Sora

Figure 8: Even with less error control for faster acceleration, our method preserves overall structural consistency, with only detail variations.

Effectiveness of threshold selection As shown in Table 2, we evaluate the acceleration performance of our method under different expansion thresholds. When accelerating different base models, generation quality declines sharply before the optimal threshold but stabilizes afterward. This trend matches the denoising deviation patterns observed in our threshold search, showing that our method effectively captures each model's tolerance to deviation. Moreover, our method achieves higher SSIM than those obtained during threshold search at high thresholds, indicating that our smoothed trend estimation helps counteract the instability of denoising under high thresholds.

Table 3: Generated results using a fixed error threshold.

Model	SDXL	FLUX	Open-Sora 1.2	Wan 2.1
SSIM↑	0.742	0.891	0.849	0.719
Latency (s)↓	2.78	9.58	21.07	348.72
Speedup↑	3.46	3.01	2.15	2.78

Fixed error threshold Table 3 shows the generation results when the error threshold searched from Open-Sora is applied as a fixed threshold across different models. As the gap from the optimal threshold varies, different models exhibit varying degrees of quality degradation. Therefore, employing model-specific error thresholds ensures consistent performance of ETC across different models. Furthermore, as shown in Table 2 and Figure 8, when employing larger error thresholds for over 3× acceleration, our method still maintains reasonable similarity (SSIM > 0.65). This demonstrates that even with less error control, our consistent trend estimation preserves the overall structural integrity of the generated results.

Table 4: SSIM results at different n and α.

n	2	4	6	7	8
FLUX	0.907	0.920	0.926	0.925	0.927
Wan 2.1	0.722	0.786	0.806	0.806	0.810
α	0.3	0.4	0.5	0.6	0.7
FLUX	0.923	0.925	0.926	0.927	0.921
Wan 2.1	0.798	0.806	0.806	0.803	0.791

Sensitivity of n and α Table 4 presents the SSIM variations under different settings of n and α. For the parameter n, initiating dilation approximation during early denoising stages with high volatility leads to degraded generation consistency. Conversely, larger n provide more stable initial trend estimation but lead to marginal improvements in SSIM. This indicates that permitting a few initial denoising steps helps establish a more stable estimate of the denoising trajectory. Additionally, the results demonstrate minimal sensitivity to different α, with SSIM variations remaining within a narrow range across all tested configurations. This robustness indicates that our trend smoothing design effectively maintains the accelerated denoising trajectory aligned with the original sampling path, preventing significant deviation from the intended generation process.

Acceleration performance across different solvers Since ETC accelerates inference by estimating the model outputs, our approach is compatible with different solvers. To investigate the performance of our method under different solvers, and to examine whether the threshold is universally applicable across solvers, we conduct experiments using multiple solvers for each model.

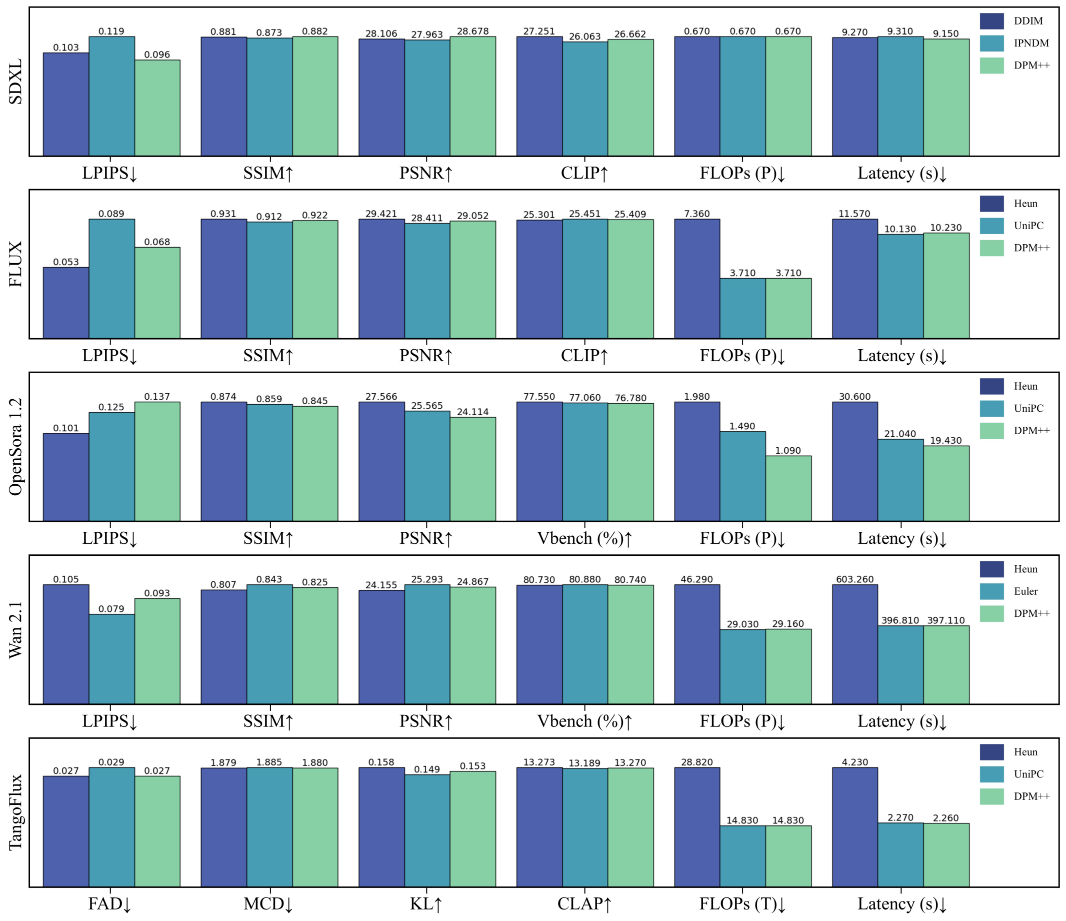

Figure 9: Quantitative results under different solvers.

For SDXL, we evaluate our method using DDIM (Song et al., 2020a), IPNDM (Liu et al., 2022) and DPM++ (Lu et al., 2025) as additional solvers. For FLUX, OpenSora1.2, and TangoFlux, we evaluate our method with Heun (Karras et al., 2022), UniPC (Zhao et al., 2023) and DPM++ as the alternative solvers. For Wan 2.1, we test our method with Euler, Heun and DPM++. All models use the thresholds specified in Table 1 and do not perform additional searches across different solvers.

As shown in Figure 9, our method maintains consistent acceleration and generation quality across different solvers without re-tuning the threshold. This indicates that the threshold we search for captures the error tolerance that prevents trajectory deviation in the model's outputs. Since this property is intrinsic to the model rather than to the choice of solver, the same threshold remains applicable as long as the model itself is unchanged. More experimental details and comprehensive results are provided in Appendix A.8.3.

5 CONCLUSION AND DISCUSSION

In this work, we proposed ETC, a training-free diffusion acceleration framework that project all historical model outputs into consistent future trends and distributing them across multiple steps within the model's tolerance limits. Experiments show that ETC preserves generative fidelity while providing substantial speedup. However, a key limitation lies in determining the maximum approximation steps per iteration, where we currently adopt a conservative adjustment strategy based only on the previous round. This restricts the attainable acceleration. A promising direction for future work is to estimate the maximum feasible approximations by evaluating the gap between accumulated errors and model-specific tolerance boundaries.

6 Ethics statement

This work adheres to the ICLR Code of Ethics. In this study, no human subjects or animal experimentation was involved. All datasets used were sourced in compliance with relevant usage guidelines, ensuring no violation of privacy. We have taken care to avoid any biases or discriminatory outcomes in our research process. No personally identifiable information was used, and no experiments were conducted that could raise privacy or security concerns. We are committed to maintaining transparency and integrity throughout the research process.

7 Reproducibility statement

We have made every effort to ensure that the results presented in this paper are reproducible. All code been made publicly available in an anonymous repository to facilitate replication and verification. The experimental setup, including model configurations and hardware details, is described in detail in the paper. We have also provided a full description of ETC, to assist others in reproducing our experiments. We believe these measures will enable other researchers to reproduce our work and further advance the field.

References

Alibaba. Flux turbo. `https://huggingface.co/alimama-creative/FLUX.1-Turbo-Alpha`, 2024.

Andreas Blattmann, Robin Rombach, Huan Ling, Tim Dockhorn, Seung Wook Kim, Sanja Fidler, and Karsten Kreis. Align your latents: High-resolution video synthesis with latent diffusion models. In *Proceedings of the IEEE/CVF conference on computer vision and pattern recognition*, pp. 22563–22575, 2023.

Pengtao Chen, Mingzhu Shen, Peng Ye, Jianjian Cao, Chongjun Tu, Christos-Savvas Bouganis, Yiren Zhao, and Tao Chen. δ-dit: A training-free acceleration method tailored for diffusion transformers, 2024b. *URL https://arxiv. org/abs/2406.01125*.

Jade Copet, Felix Kreuk, Itai Gat, Tal Remez, David Kant, Gabriel Synnaeve, Yossi Adi, and Alexandre Défossez. Simple and controllable music generation. *Advances in Neural Information Processing Systems*, 36:47704–47720, 2023.

Tri Dao, Dan Fu, Stefano Ermon, Atri Rudra, and Christopher Ré. Flashattention: Fast and memory-efficient exact attention with io-awareness. *Advances in neural information processing systems*, 35:16344–16359, 2022.

William Feller et al. *An introduction to probability theory and its applications*, volume 963. Wiley New York, 1971.

Jonathan Ho, Ajay Jain, and Pieter Abbeel. Denoising diffusion probabilistic models. *Advances in neural information processing systems*, 33:6840–6851, 2020.

Ziqi Huang, Yinan He, Jiashuo Yu, Fan Zhang, Chenyang Si, Yuming Jiang, Yuanhan Zhang, Tianxing Wu, Qingyang Jin, Nattapol Chanpaisit, et al. Vbench: Comprehensive benchmark suite for video generative models. In *Proceedings of the IEEE/CVF Conference on Computer Vision and Pattern Recognition*, pp. 21807–21818, 2024.

Chia-Yu Hung, Navonil Majumder, Zhifeng Kong, Ambuj Mehrish, Amir Ali Bagherzadeh, Chuan Li, Rafael Valle, Bryan Catanzaro, and Soujanya Poria. Tangoflux: Super fast and faithful text to audio generation with flow matching and clap-ranked preference optimization. *arXiv preprint arXiv:2412.21037*, 2024.

Ting Jiang, Yixiao Wang, Hancheng Ye, Zishan Shao, Jingwei Sun, Jingyang Zhang, Zekai Chen, Jianyi Zhang, Yiran Chen, and Hai Li. Sada: Stability-guided adaptive diffusion acceleration. *arXiv preprint arXiv:2507.17135*, 2025.

Tero Karras, Miika Aittala, Timo Aila, and Samuli Laine. Elucidating the design space of diffusion-based generative models. *Advances in neural information processing systems*, 35:26565–26577, 2022.

Kevin Kilgour, Mauricio Zuluaga, Dominik Roblek, and Matthew Sharifi. Fr\'echet audio distance: A metric for evaluating music enhancement algorithms. *arXiv preprint arXiv:1812.08466*, 2018.

Chris Dongjoo Kim, Byeongchang Kim, Hyunmin Lee, and Gunhee Kim. Audiocaps: Generating captions for audios in the wild. In *NAACL-HLT*, 2019.

Khaled Koutini, Jan Schlüter, Hamid Eghbal-Zadeh, and Gerhard Widmer. Efficient training of audio transformers with patchout. *arXiv preprint arXiv:2110.05069*, 2021.

Robert Kubichek. Mel-cepstral distance measure for objective speech quality assessment. In *Proceedings of IEEE pacific rim conference on communications computers and signal processing*, volume 1, pp. 125–128. IEEE, 1993.

Black Forest Labs. Flux. `https://github.com/black-forest-labs/flux`, 2024.

Haeil Lee, Hansang Lee, Seoyeon Gye, and Junmo Kim. Beta sampling is all you need: Efficient image generation strategy for diffusion models using stepwise spectral analysis. In *2025 IEEE/CVF Winter Conference on Applications of Computer Vision (WACV)*, pp. 4215–4224. IEEE, 2025.

Shanchuan Lin, Anran Wang, and Xiao Yang. Sdxl-lightning: Progressive adversarial diffusion distillation, 2024.

Tsung-Yi Lin, Michael Maire, Serge Belongie, James Hays, Pietro Perona, Deva Ramanan, Piotr Dollár, and C Lawrence Zitnick. Microsoft coco: Common objects in context. In *European conference on computer vision*, pp. 740–755. Springer, 2014.

Yaron Lipman, Ricky TQ Chen, Heli Ben-Hamu, Maximilian Nickel, and Matt Le. Flow matching for generative modeling. *arXiv preprint arXiv:2210.02747*, 2022.

Feng Liu, Shiwei Zhang, Xiaofeng Wang, Yujie Wei, Haonan Qiu, Yuzhong Zhao, Yingya Zhang, Qixiang Ye, and Fang Wan. Timestep embedding tells: It's time to cache for video diffusion model. In *Proceedings of the Computer Vision and Pattern Recognition Conference*, pp. 7353–7363, 2025a.

Haozhe Liu, Wentian Zhang, Jinheng Xie, Francesco Faccio, Mengmeng Xu, Tao Xiang, Mike Zheng Shou, Juan-Manuel Perez-Rua, and Jürgen Schmidhuber. Faster diffusion via temporal attention decomposition. *Transactions on Machine Learning Research*, 2025b. URL `https://openreview.net/forum?id=xXs2GKXPnH`.

Luping Liu, Yi Ren, Zhijie Lin, and Zhou Zhao. Pseudo numerical methods for diffusion models on manifolds. *arXiv preprint arXiv:2202.09778*, 2022.

Cheng Lu, Yuhao Zhou, Fan Bao, Jianfei Chen, Chongxuan Li, and Jun Zhu. Dpm-solver++: Fast solver for guided sampling of diffusion probabilistic models. *Machine Intelligence Research*, pp. 1–22, 2025.

Simian Luo, Yiqin Tan, Longbo Huang, Jian Li, and Hang Zhao. Latent consistency models: Synthesizing high-resolution images with few-step inference. *arXiv preprint arXiv:2310.04378*, 2023.

Zhengyao Lv, Chenyang Si, Junhao Song, Zhenyu Yang, Yu Qiao, Ziwei Liu, and Kwan-Yee K. Wong. Fastercache: Training-free video diffusion model acceleration with high quality. In *arxiv*, 2024.

Xinyin Ma, Gongfan Fang, Michael Bi Mi, and Xinchao Wang. Learning-to-cache: Accelerating diffusion transformer via layer caching. *Advances in Neural Information Processing Systems*, 37: 133282–133304, 2024a.

Xinyin Ma, Gongfan Fang, and Xinchao Wang. Deepcache: Accelerating diffusion models for free. In *Proceedings of the IEEE/CVF conference on computer vision and pattern recognition*, pp. 15762–15772, 2024b.

Zehong Ma, Longhui Wei, Feng Wang, Shiliang Zhang, and Qi Tian. Magcache: Fast video generation with magnitude-aware cache. *arXiv preprint arXiv:2506.09045*, 2025.

William Peebles and Saining Xie. Scalable diffusion models with transformers. In *Proceedings of the IEEE/CVF international conference on computer vision*, pp. 4195–4205, 2023.

Dustin Podell, Zion English, Kyle Lacey, Andreas Blattmann, Tim Dockhorn, Jonas Müller, Joe Penna, and Robin Rombach. Sdxl: Improving latent diffusion models for high-resolution image synthesis. *arXiv preprint arXiv:2307.01952*, 2023.

Alec Radford, Jong Wook Kim, Chris Hallacy, Aditya Ramesh, Gabriel Goh, Sandhini Agarwal, Girish Sastry, Amanda Askell, Pamela Mishkin, Jack Clark, et al. Learning transferable visual models from natural language supervision. In *International conference on machine learning*, pp. 8748–8763. PmLR, 2021.

Robin Rombach, Andreas Blattmann, Dominik Lorenz, Patrick Esser, and Björn Ommer. High-resolution image synthesis with latent diffusion models. In *Proceedings of the IEEE/CVF conference on computer vision and pattern recognition*, pp. 10684–10695, 2022.

Olaf Ronneberger, Philipp Fischer, and Thomas Brox. U-net: Convolutional networks for biomedical image segmentation. In *International Conference on Medical image computing and computer-assisted intervention*, pp. 234–241. Springer, 2015.

Tim Salimans and Jonathan Ho. Progressive distillation for fast sampling of diffusion models. *arXiv preprint arXiv:2202.00512*, 2022.

Jascha Sohl-Dickstein, Eric Weiss, Niru Maheswaranathan, and Surya Ganguli. Deep unsupervised learning using nonequilibrium thermodynamics. In *International conference on machine learning*, pp. 2256–2265. pmlr, 2015.

Jiaming Song, Chenlin Meng, and Stefano Ermon. Denoising diffusion implicit models. *arXiv preprint arXiv:2010.02502*, 2020a.

Yang Song and Stefano Ermon. Generative modeling by estimating gradients of the data distribution. *Advances in neural information processing systems*, 32, 2019.

Yang Song, Jascha Sohl-Dickstein, Diederik P Kingma, Abhishek Kumar, Stefano Ermon, and Ben Poole. Score-based generative modeling through stochastic differential equations. *arXiv preprint arXiv:2011.13456*, 2020b.

Samuel Stanton, Pavel Izmailov, Polina Kirichenko, Alexander A Alemi, and Andrew G Wilson. Does knowledge distillation really work? *Advances in neural information processing systems*, 34:6906–6919, 2021.

Charles Truong, Laurent Oudre, and Nicolas Vayatis. Selective review of offline change point detection methods. *Signal Processing*, 167:107299, 2020.

Ashish Vaswani, Noam Shazeer, Niki Parmar, Jakob Uszkoreit, Llion Jones, Aidan N Gomez, Łukasz Kaiser, and Illia Polosukhin. Attention is all you need. *Advances in neural information processing systems*, 30, 2017.

Team Wan, Ang Wang, Baole Ai, Bin Wen, Chaojie Mao, Chen-Wei Xie, Di Chen, Feiwu Yu, Haiming Zhao, Jianxiao Yang, et al. Wan: Open and advanced large-scale video generative models. *arXiv preprint arXiv:2503.20314*, 2025.

Alex Jinpeng Wang, Dongxing Mao, Jiawei Zhang, Weiming Han, Zhuobai Dong, Linjie Li, Yiqi Lin, Zhengyuan Yang, Libo Qin, Fuwei Zhang, et al. Textatlas5m: A large-scale dataset for dense text image generation. *arXiv preprint arXiv:2502.07870*, 2025.

Wei Wu, Qingnan Fan, Shuai Qin, Hong Gu, Ruoyu Zhao, and Antoni B Chan. Freediff: Progressive frequency truncation for image editing with diffusion models. In *European Conference on Computer Vision*, pp. 194–209. Springer, 2024.

Yusong Wu, Ke Chen, Tianyu Zhang, Yuchen Hui, Taylor Berg-Kirkpatrick, and Shlomo Dubnov. Large-scale contrastive language-audio pretraining with feature fusion and keyword-to-caption augmentation. In *ICASSP 2023-2023 IEEE International Conference on Acoustics, Speech and Signal Processing (ICASSP)*, pp. 1–5. IEEE, 2023.

Zhantao Yang, Ruili Feng, Han Zhang, Yujun Shen, Kai Zhu, Lianghua Huang, Yifei Zhang, Yu Liu, Deli Zhao, Jingren Zhou, et al. Lipschitz singularities in diffusion models. In *The Twelfth International Conference on Learning Representations*, 2023.

Hancheng Ye, Jiakang Yuan, Renqiu Xia, Xiangchao Yan, Tao Chen, Junchi Yan, Botian Shi, and Bo Zhang. Training-free adaptive diffusion with bounded difference approximation strategy. *Advances in Neural Information Processing Systems*, 37:306–332, 2024.

Richard Zhang, Phillip Isola, Alexei A. Efros, Eli Shechtman, and Oliver Wang. The unreasonable effectiveness of deep features as a perceptual metric, 2018. URL `https://arxiv.org/abs/1801.03924`.

Sixian Zhang, Bohan Wang, Junqiang Wu, Yan Li, Tingting Gao, Di Zhang, and Zhongyuan Wang. Learning multi-dimensional human preference for text-to-image generation. In *Proceedings of the IEEE/CVF Conference on Computer Vision and Pattern Recognition*, pp. 8018–8027, 2024.

Wenliang Zhao, Lujia Bai, Yongming Rao, Jie Zhou, and Jiwen Lu. Unipc: A unified predictor-corrector framework for fast sampling of diffusion models. *Advances in Neural Information Processing Systems*, 36:49842–49869, 2023.

Zangwei Zheng, Xiangyu Peng, Tianji Yang, Chenhui Shen, Shenggui Li, Hongxin Liu, Yukun Zhou, Tianyi Li, and Yang You. Open-sora: Democratizing efficient video production for all, March 2024. URL `https://github.com/hpcaitech/Open-Sora`.

Chang Zou, Xuyang Liu, Ting Liu, Siteng Huang, and Linfeng Zhang. Accelerating diffusion transformers with token-wise feature caching. *arXiv preprint arXiv:2410.05317*, 2024.

A Appendix

A.1 Error estimation induced by consistent trend predictor

A.1.1 A generalized formula for model inference k steps

Suppose we inference once to obtain model output $\epsilon_\theta(x_t, t, c)$ from the latent x_t, the denoised formula is as follows:

$$x_{t-1} = f(t-1) \cdot x_t - g(t-1) \cdot \epsilon_\theta(x_t, t, c) \tag{9}$$

Similarly, we can obtain the following formula after the second denoising and substituting Equation 9:

$$\begin{aligned} x_{t-2} &= f(t-2) \cdot x_{t-2} - g(t-2) \cdot \epsilon_\theta(x_{t-1}, t-1, c) \\ &= f(t-2) \cdot f(t-1) \cdot x_t - f(t-2) \cdot g(t-1) \cdot \epsilon_\theta(x_t, t, c) - g(t-2) \cdot \epsilon_\theta(x_{t-1}, t-1, c). \end{aligned} \tag{10}$$

By analogy, we can obtain the following results after sampling k times using the model output:

$$\begin{aligned} x_{t-k} = &\prod_{\mathrm{j}=t-k}^{t-1} f(j) \cdot x_t - g(t-k) \cdot \epsilon_\theta(x_{t-k+1}, t-k+1, c) \\ &- \sum_{m=0}^{k-2} \left(\left(\prod_{j=t-k}^{t-k+m} f(j)\right) \cdot g(t-k+m+1) \cdot \epsilon_\theta(x_{t-k+m+2}, t-k+m+2, c)\right). \end{aligned} \tag{11}$$

A.1.2 Cumulative error caused by using estimated trends for the first time

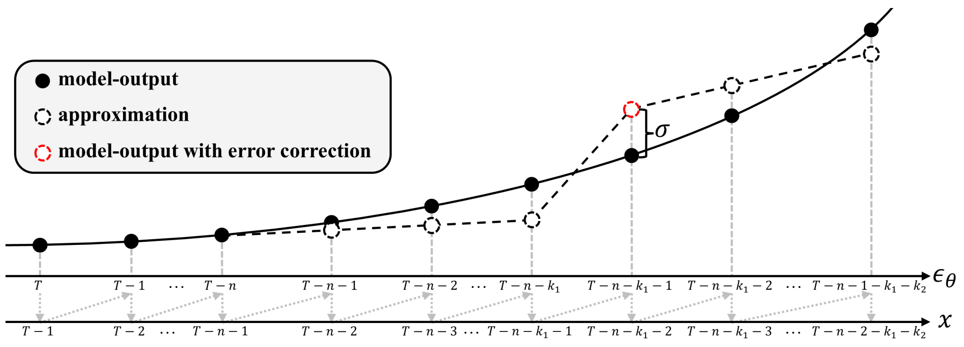

Figure 10: Error accumulation for k times approximation used after model inference n times.

Assumptions As shown in Figure 10, we make the assumptions that:

(1) The timestep of the denoising process decreases from T to 0;

(2) Let $d_{t_2}^{t_1} = \epsilon_\theta(x_{t_2}, t_2, c) - \epsilon_\theta(x_{t_1}, t_1, c)$;

(3) Estimated trend is utilized for denoising after performing model inference n times.

Initial approximate trend When the model performs inference twice first and then the outputs are used to calculate the estimated trend, the formula is as follows:

$$\Delta_{T-2} = \epsilon_\theta(x_{T-1}, T-1, c) - \epsilon_\theta(x_T, T, c) = d_{T-1}^{T}. \tag{12}$$

The second estimated trend formulation is as follows:

$$\Delta_{T-3} = (1-\alpha) \cdot \Delta_{T-2} + \alpha \cdot d_{T-2}^{T-1} = (1-\alpha) \cdot d_{T-1}^{T} + \alpha \cdot d_{T-2}^{T-1}. \tag{13}$$

The third estimated trend formulation is as follows:

$$\begin{aligned} \Delta_{T-4} &= (1-\alpha) \cdot \Delta_{T-3} + \alpha \cdot d_{T-3}^{T-2} = (1-\alpha) \cdot ((1-\alpha) \cdot d_{T-1}^{T} + \alpha \cdot d_{T-2}^{T-1}) + \alpha \cdot d_{T-3}^{T-2} \\ &= (1-\alpha)^2 \cdot d_{T-1}^{T} + \alpha \cdot (1-\alpha) \cdot d_{T-2}^{T-1} + \alpha \cdot d_{T-3}^{T-2} \end{aligned}. \tag{14}$$

By analogy, we can obtain the following estimated trend for the n^{th} iteration:

$$\Delta_{T-n-1} = (1-\alpha)^{n-1} \cdot d_{T-1}^{T} + \alpha \sum_{m=0}^{n-2} (1-\alpha)^m \cdot d_{T-n+m}^{T-n+m+1}. \tag{15}$$

Cumulative error To improve readability, we set $\epsilon_\theta(x_t) = \epsilon_\theta(x_t, t, c)$. Starting from x_{T-n-1}, the formulation for $x_{T-n-1-k_1}$ based on the estimated trend and Equation 11 is as follows:

$$\begin{aligned} x'_{T-n-1-k_1} = & \prod_{j=T-n-1-k_1}^{T-n-2} f(j) \cdot x_{T-n-1} - g(T-n-1-k_1) \cdot (\epsilon_\theta(x_{T-n}) + \Delta_{T-n-1}) \\ & - \sum_{m=0}^{k_1-2} ((\prod_{j=T-n-1-k_1}^{T-n-1-k_1+m} f(j)) \cdot g(T-n-k_1+m) \cdot (\epsilon_\theta(x_{T-n}) + \frac{k_1-m-1}{k_1} \Delta_{T-n-1})). \end{aligned} \tag{16}$$

The cumulative error is as follows:

$$\begin{aligned} error &= \|x_{T-n-1-k_1} - x'_{T-n-1-k_1}\| \\ &= \|g(T-n-1-k_1) \cdot (\Delta_{T-n-1} - d_{T-n-k_1}^{T-n}) \\ &+ \sum_{m=0}^{k_1-2} ((\prod_{j=T-n-1-k_1}^{T-n-1-k_1+m} f(j)) \cdot g(T-n-k_1+m) \cdot (\frac{k_1-m-1}{k_1} \Delta_{T-n-1} - d_{T-n-k_1+m+1}^{T-n}))\|. \end{aligned} \tag{17}$$

Since $f \leq 1$ and $g \leq 1$, we can get the formulation below:

$$\begin{aligned} error &\leq \|(\Delta_{T-n-1} - d_{T-n-k_1}^{T-n}) + (\frac{k_1-m-1}{k_1} \Delta_{T-n-1} - d_{T-n-k_1+m+1}^{T-n})\| \\ &= \| \sum_{m=0}^{k_1-1} (\frac{k_1-m}{k_1} \Delta_{T-n-1} - d_{T-n-k_1+m}^{T-n})\|. \end{aligned} \tag{18}$$

Substituting Equation 15 into Equation 18, we obtain the following upper bound on the error:

$$error \leq \| \sum_{m=0}^{k_1-1} (\frac{(k_1-m)(1-\alpha)^{n-1}}{k_1} \cdot d_{T-1}^{T} + \frac{\alpha(k_1-m)}{k_1} \sum_{j=0}^{n-2} (1-\alpha)^j \cdot d_{T-n+j}^{T-n+j+1} - d_{T-n-k_1+m}^{T-n})\|. \tag{19}$$

A.1.3 Error accumulation in the next round

Assumptions As shown in Figure 10, we make the assumptions that:

(1) To correct the cumulative error, the model output $\epsilon^*_\theta(x_{T-n-k_1-1}) = \epsilon_\theta(x_{T-n-k_1-1}) + \sigma_1$. After a single model inference, the obtained x_{T-n-k_1-2} exhibits no error.

Updated approximate trend After correcting the cumulative error using a single model inference, we update the formula for estimated trend as follows:

$$\begin{aligned} \Delta_{T-n-2-k_1} &= (1-\alpha) \cdot \Delta_{T-n-1} + \alpha \cdot ((\epsilon_\theta(x_{T-n-k_1-1}) + \sigma_1) - (\epsilon_\theta(x_{T-n}) + \Delta_{T-n-1})) \\ &= (1-2\alpha) \cdot \Delta_{T-n-1} + \alpha \cdot (d_{T-n-k_1-1}^{T-n} + \sigma_1). \end{aligned} \tag{20}$$

Cumulative error To improve readability, we omit the arguments of f and g. Starting from $x_{T-n-2-k_1}$, the formulation for $x_{T-n-2-k_1-k_2}$ based on the estimated trend and Equation 11 is:

$$\begin{aligned} x'_{T-n-2-k_1-k_2} = & \prod f \cdot x_{T-n-2-k_1} - g \cdot (\epsilon_\theta(x_{T-n-1-k_1}) + \sigma_1 + \Delta_{T-n-2-k_1}) \\ & - \sum_{m=0}^{k_2-2} ((\prod f) \cdot g \cdot (\epsilon_\theta(x_{T-n-1-k_1}) + \sigma_1 + \frac{k_2-m-1}{k_2} \Delta_{T-n-2-k_1})). \end{aligned} \tag{21}$$

The cumulative error is as follows:

$$\begin{aligned} error = \|x_{T-n-2-k_1-k_2} - x'_{T-n-2-k_1-k_2}\| = & \|g \cdot (\sigma_1 + \Delta_{T-n-2-k_1} - d_{T-n-1-k_1-k_2}^{T-n-1-k_1}) \\ & + \sum_{m=0}^{k_2-2} ((\prod f) \cdot g \cdot (\sigma_1 + \frac{k_2-m-1}{k_2} \Delta_{T-n-2-k_1} - d_{T-n-k_1-k_2+m}^{T-n-1-k_1}))\|. \end{aligned} \tag{22}$$

Since $f \leq 1$ and $g \leq 1$, we can get the formulation below:

$$\begin{aligned} error &\leq \|(\sigma_1 + \Delta_{T-n-2-k_1} - d^{T-n-1-k_1}_{T-n-1-k_1-k_2}) + (\sigma_1 + \frac{k_2-m-1}{k_2}\Delta_{T-n-2-k_1} - d^{T-n-1-k_1}_{T-n-k_1-k_2+m})\| \\ &= \|\sum_{m=0}^{k_2-1}(\sigma_1 + \frac{k_2-m}{k_2}\Delta_{T-n-2-k_1} - d^{T-n-1-k_1}_{T-n-1-k_1-k_2+m})\|. \end{aligned} \tag{23}$$

Substituting Equation 20 into Equation 23, we obtain the following upper bound on the error:

$$\begin{aligned} error \leq \| \sum_{m=0}^{k_2-1} (&\frac{(k_2-m)(1-2\alpha)(1-\alpha)^{n-1}}{k_2} \cdot d^{T}_{T-1} + \frac{\alpha(k_2-m)(1-2\alpha)}{k_2}\sum_{j=0}^{n-2}(1-\alpha)^j \cdot d^{T-n+j+1}_{T-n+j} \\ &+ \frac{\alpha(k_2-m)}{k_2}\cdot d^{T-n}_{T-n-k_1-1} + \frac{k_2+\alpha(k_2-m)}{k_2}\cdot\sigma_1 - d^{T-n-1-k_1}_{T-n-1-k\_k_2+m})\|. \end{aligned} \tag{24}$$

A.1.4 Accumulation of errors throughout the process

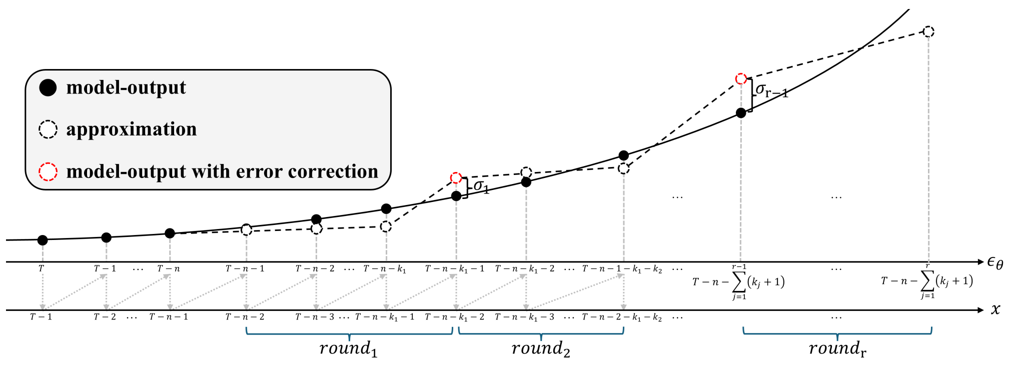

Figure 11: Error accumulation throughout the denoising process.

Assumptions As shown in Figure 11, we make the assumptions that:

(1) A total of r rounds of approximations were performed, with k_i approximations per round, and the difference between the outputs obtained using model inference and the model outputs under no error for each round is σ_{i-1}, where $i = 1, ..., r$.

Approximate trend at each round By analogy, we can obtain the following formulation for the estimated trend used in the r^{th} round:

$$\Delta_{T-n-1-\sum_{m=1}^{r-1}(k_m+1)} = (1-2\alpha)^{r-1}\Delta_{T-n-1} + \alpha\sum_{m=1}^{r-1}((1-2\alpha)^{r-m-1}(d^{T-n-\sum_{j=1}^{m-1}(k_j+1)}_{T-n-\sum_{j=1}^{m}k_j+1} + \sigma_m)) \tag{25}$$

Cumulative error By analogy, we can obtain the following formulation for the cumulative error in the r^{th} round:

$$\begin{aligned} error_r &\leq \|\sum_{m=0}^{k_r-1}(\sigma_{r-1} + \frac{k_r-m}{k_r}\Delta_{T-n-1-\sum_{j=1}^{r-1}(k_j+1)} - d^{T-n-\sum_{j=1}^{r-1}(k_j+1)}_{T-n-\sum_{j=1}^{r-1}(k_j+1)-k_r+m})\| \\ &= \|\sum_{m=0}^{k_r-1}(\sigma_{r-1} + \frac{(k_r-m)(1-2\alpha)^{r-1}}{k_r}\Delta_{T-n-1} \\ &\quad + \frac{\alpha(k_r-m)}{k_r}\sum_{j=1}^{r-1}((1-2\alpha)^{r-j-1}(d^{T-n-\sum_{l=1}^{j-1}(k_l+1)}_{T-n-\sum_{l=1}^{j}(k_l+1)} + \sigma_j)) - d^{T-n-\sum_{j=1}^{r-1}(k_j+1)}_{T-n-\sum_{j=1}^{r-1}(k_j+1)-k_r+m})\| \end{aligned} \tag{26}$$

Substituting Equation 15 into Equation 26, we obtain the following upper bound on the error:

$$
\begin{aligned}
error_r \leq \| \sum_{m=0}^{k_r-1} ((\sigma_{r-1} + \frac{\alpha(k_r-m)}{k_r} \sum_{j=1}^{r-1} (1-2\alpha)^{r-j-1} \cdot \sigma_j) \\
+ (\frac{(k_r-m)(1-2\alpha)^{r-1}(1-\alpha)^{n-1}}{k_r} \cdot d_{T-1}^{T} + \frac{\alpha(k_r-m)(1-2\alpha)^{r-1}}{k_r} \sum_{j=0}^{n-2} (1-\alpha)^{j} \cdot d_{T-n+j}^{T-n+j+1} \\
+ \frac{\alpha(k_r-m)}{k_r} \sum_{j=1}^{r-1} (1-2\alpha)^{r-j-1} \cdot d_{T-n-\sum_{l=1}^{j}(k_l+1)}^{T-n-\sum_{l=1}^{j-1}(k_l+1)} - d_{T-n-\sum_{j=1}^{m}(k_j+1)-k_r+m}^{T-n-\sum_{j=1}^{m-1}(k_j+1)})\|
\end{aligned}
\tag{27}
$$

As can be seen, we approximate the future trend at each step by a weighted combination of the historical trend and the error-correction.

A.2 Trajectory continuity of diffusion processes

A.2.1 Continuity of the forward process

By the definition of the forward process in diffusion models, the variable at timestep t is given by:

$$x_t = \alpha(t) \cdot x_0 + \beta(t) \cdot \epsilon, \tag{28}$$

where $\alpha(t)$ and $\beta(t)$ are noise scheduling coefficients. Taking expectation over $x_0 \sim p(x_0)$,$\epsilon \sim \mathcal{N}(0, I)$, and $t \sim \text{Uniform}(1, ..., T)$, we get:

$$\mathbb{E}_{x_0,\epsilon,t} = \mathbb{E}[\mathbb{E}_{x_0}[\alpha(t) \cdot x_0] + \mathbb{E}_{\epsilon}[\beta(t) \cdot \epsilon]]. \tag{29}$$

Since $\epsilon \sim \mathcal{N}(0, I)$, we have $\mathbb{E}[\epsilon] = 0$, and thus:

$$\mathbb{E}_{x_0,\epsilon,t} = \mathbb{E}_t[\alpha(t) \cdot \mathbb{E}_{x_0}[x_0]] = \alpha(t) \cdot \mathbb{E}_{x_0}[x_0]. \tag{30}$$

From Equation 30, we know that the trajectory x_t is continuous in expectation. Consequently, the empirical average x_t also exhibits continuity by the law of large numbers (Feller et al., 1971).

A.2.2 Continuity of the backward process

Different mathematical definitions of the denoising process The denoising process can be defined through various mathematical frameworks. Stochastic differential equation (SDE) (Song et al., 2020b) defines the process as follows:

$$dx = \left[-\frac{1}{2}\beta(t)x - \nabla_{x_t} \log p_t(x_t)\right] dt + \sqrt{\beta(t)} d\bar{w}, \tag{31}$$

where $\nabla_{x_t} \log p_t(x_t)$ denotes the log-likelihood gradient and $d\bar{w}$ represents the standard Wiener process. Ordinary differential equation (ODE) removes the term $d\bar{w}$ from Equation 31, offering a more stable denoising process that mitigates fluctuations inherent in stochastic processes. Flow matching (Lipman et al., 2022) proposes a deterministic approach to denoising by learning data flows, mathematically described as follows:

$$dx = v(x_t, t)dt, \tag{32}$$

where $v(x_t, t)$ represents the flow function that governs the evolution of data toward the target distribution over time.

ϵ-prediction in sde and ode. The noise prediction model (Ho et al., 2020; Song et al., 2020a) is trained to estimate the noise contained in x_t, which is proved to be equivalent to estimating the log-likelihood gradient by Ho et al. (2020). Given the origin data x_0, the forward noising process is defined as:

$$x_t = \sqrt{\bar{\alpha}_t} x_0 + \sqrt{1-\bar{\alpha}_t}\epsilon, \quad \bar{\alpha}_t = \prod_{i=1}^{t}(1-\beta_i), \tag{33}$$

where $\beta \in (0, 1)$ and $\epsilon \sim N(0, I)$. Then the network $\epsilon_\theta(x, t)$ is trained with the standard mean-squared error (MSE) objective:

$$\mathcal{L}(\theta) = \mathbb{E}_{x_0,\epsilon,t}[||\epsilon - \epsilon_\theta(x_t, t)||^2], \quad x_t = \sqrt{\bar{\alpha}_t} x_0 + \sqrt{1-\bar{\alpha}_t}\epsilon. \tag{34}$$

During the denoising stage, the next time-step x_{t-1} can be obtained from x_t as:

$$x_{t-1} = \sqrt{\bar{\alpha}_{t-1}}(\frac{x_t - \sqrt{1-\bar{\alpha}_t}\epsilon_\theta(x_t, t)}{\sqrt{\bar{\alpha}_t}}) + \sqrt{1-\bar{\alpha}_t}\epsilon_\theta(x_t, t). \tag{35}$$

Taking expectation over $x_t \sim p(x_t)$ and $t \sim$Uniform$(1, ..., T)$, we get:

$$\begin{aligned}\mathbb{E}_{x_t,\epsilon_\theta,t} &= \mathbb{E}[\mathbb{E}_{x_t}[\frac{\sqrt{\bar{\alpha}_{t-1}}}{\sqrt{\bar{\alpha}_t}}x_t] + \mathbb{E}_{\epsilon_\theta}[\sqrt{1-\bar{\alpha}_t}(1 - \frac{\sqrt{\bar{\alpha}_{t-1}}}{\sqrt{\bar{\alpha}_t}})\epsilon_\theta(x_t, t)]] \\ &= \frac{\sqrt{\bar{\alpha}_{t-1}}}{\sqrt{\bar{\alpha}_t}} \cdot \mathbb{E}_{x_t}[x_t] + \sqrt{1-\bar{\alpha}_t}(1 - \frac{\sqrt{\bar{\alpha}_{t-1}}}{\sqrt{\bar{\alpha}_t}}) \cdot \mathbb{E}_{\epsilon_\theta}[\epsilon_\theta(x_t, t)]\end{aligned} \tag{36}$$

Suppose θ minimizes $\mathcal{L}$, and the training is sufficiently converged, then $\epsilon_\theta(x_t, t) \approx \epsilon \sim \mathcal{N}(0, I)$. Since $\epsilon_\theta \sim \mathcal{N}(0, I)$, we have $\mathbb{E}[\epsilon_\theta] = 0$, and thus:

$$\mathbb{E}_{x_t,\epsilon_\theta,t} = \mathbb{E}_t[\frac{\sqrt{\bar{\alpha}_{t-1}}}{\sqrt{\bar{\alpha}_t}} \cdot \mathbb{E}_{x_t}[x_t]] = \frac{\sqrt{\bar{\alpha}_{t-1}}}{\sqrt{\bar{\alpha}_t}} \cdot \mathbb{E}_{x_t}[x_t] \tag{37}$$

v-prediction in flow matching. Flow matching defines a vector field v that guides the data from the initial distribution x_0 toward the target distribution x_T. Specifically, the linear interpolation path from x_0 to x_T is:

$$x_t = (1 - \frac{t}{T})x_0 + \frac{t}{T}x_T, \quad x_T \sim \mathcal{N}(0, I), \quad t \sim \text{Uniform}(1, ..., T). \tag{38}$$

The vector field v is defined as:

$$v = \frac{dx}{dt} = -x_0 + x_T = x_T - x_0. \tag{39}$$

Then the network $v_\theta(x, t)$ is trained with the standard mean-squared error (MSE) objective:

$$\mathcal{L}(\theta) = \mathbb{E}_{x_0,x_T,v,t}[||v - v_\theta(x_t, t)||^2], \quad v = x_T - x_0. \tag{40}$$

During the denoising stage, the next time-step x_{t-1} can be obtained from x_t as:

$$x_{t-1} = x_t - (\frac{t}{T} - \frac{t-1}{T})v_\theta(x_t, t) = x_t - \frac{1}{T}v_\theta(x_t, t), \tag{41}$$

Taking expectation over $x_t \sim p(x_t)$ and $t \sim$Uniform$(1, ..., T)$, we get:

$$\mathbb{E}_{x_t,v_\theta,t} = \mathbb{E}[\mathbb{E}_{x_t}[x_t] - \mathbb{E}_{v_\theta}[\frac{1}{T}v_\theta]] = \mathbb{E}_{x_t}[x_t] - \frac{1}{T}\mathbb{E}_{v_\theta}[v_\theta(x_t, t)] \tag{42}$$

Suppose θ minimizes $\mathcal{L}$, and the training is sufficiently converged, then $v_\theta(x_t, t) \approx v$.

$$\begin{aligned}\mathbb{E}_{x_t,v_\theta,t} &= \mathbb{E}[\mathbb{E}_{x_t}[x_t] - \mathbb{E}_{v_\theta}[\frac{1}{T}v_\theta]] = \mathbb{E}[\mathbb{E}_{x_t}[x_t] - \mathbb{E}[\frac{1}{T}(x_T - x_0)]] \\ &= \mathbb{E}[\mathbb{E}_{x_t}[x_t] - \mathbb{E}[\frac{1}{T}(x_T - \frac{T}{T-t}(x_t - \frac{t}{T}x_T))]]\end{aligned} \tag{43}$$

Since $x_T \sim \mathcal{N}(0, I)$,we have $\mathbb{E}[x_T] = 0$, and thus:

$$\mathbb{E}_{x_t,v_\theta,t} = \mathbb{E}[\mathbb{E}_{x_t}[x_t] + \mathbb{E}_{x_t}[\frac{1}{T-t}x_t]] = \mathbb{E}_t[(1 + \frac{1}{T-t})\mathbb{E}_{x_t}[x_t]] = \frac{T-t+1}{T-t} \cdot \mathbb{E}_{x_t}[x_t]. \tag{44}$$

From Equation 37 and Equation 44, a well-trained denoiser permits the sampling trajectory from x_t to x_0 continuous in expectation. Consequently, the empirical average x_t also exhibits continuity by the law of large numbers (Feller et al., 1971).

However, as shown in Figure 12 (b) and (c), the mean of the model's output varies across timesteps during inference. This occurs because different timesteps correspond to different noise levels and contain different amounts of information, leading to variations in the predicted values. Consequently, as implied by Equations Equation 36 and Equation 42, under a fixed scheduler, the differences in the denoising trajectory are determined by the model θ.

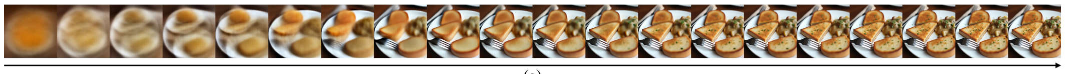

(a)

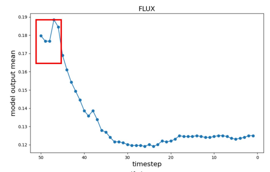

(b)

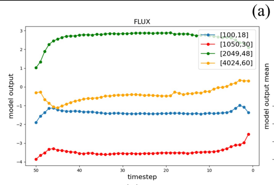

(c)

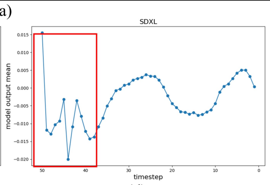

(d)

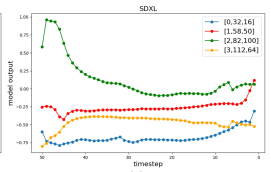

(e)

Figure 12: Visualization of fluctuation and stabilization phases during denoising. Subfigure (a) shows the results obtained at each timestep by directly sampling x_0 from model outputs. Subfigures (b) and (d) present the mean output curves of FLUX and SDXL across timesteps. Subfigures (c) and (e) show the output trajectories at four selected latent points for FLUX and SDXL, respectively.

A.3 FLUCTUATION AND STABILIZATION PHASES OF MODEL OUTPUTS DURING DENOISING

Figure 12(a) visualizes the denoising process during the semantic planning phase and the fidelity refinement phase. At the beginning of the denoising process, the model gradually constructs the main semantic components of the image, for example, first the plate appears, then the bread. Once the global structure aligns with the semantic intent, subsequent denoising shifts toward refining details, such as adding scallions on the bread.

As analyzed in A.2.2, the evolution of the denoising process is determined by the model outputs. Therefore, we visualize the timestep-wise mean of the model outputs for SDXL (ϵ-prediction) and FLUX (v-prediction). As shown in Figure 12(b) and (d), the mean outputs exhibit pronounced fluctuations in the early denoising steps and then gradually stabilize, which is consistent with the behavior observed in Figure 12(a).

Figure 12(c) and (e) further plot the output differences between adjacent timesteps at four selected latent positions for FLUX and SDXL. In the refinement phase, these differences become stable, indicating a consistent output trend. This motivates us to apply approximation-based acceleration during this stable stage.

A.4 PROOF OF LIPSCHITZ CONTINUITY OF ϵ_θ

Based on Equation 28, we obtain the following formulation for the noise at timestep t:

$$\epsilon = \frac{1}{\beta(t)}x_t - \frac{\alpha(t)}{\beta(t)}x_0. \tag{45}$$

Assuming that under the same conditions c, the corresponding x_0 remains identical across timesteps, and the trained model's outputs $\epsilon_\theta(x_t, t, c)$ at different timesteps follow Equation 45, we obtain the following formulation for the model output difference between timestep t and timestep t':

$$\begin{aligned}\epsilon_\theta(x_t, t, c) - \epsilon_\theta(x_{t'}, t', c) &= \frac{x_t - \alpha(t)x_0}{\beta(t)} - \frac{x_{t'} - \alpha(t')x_0}{\beta(t')} \\ &= \frac{x_t - x_{t'}}{\beta(t)} + \frac{x_{t'} - \alpha(t')x_0}{\beta(t)} - \frac{x_{t'} - \alpha(t')x_0}{\beta(t')} + \frac{-\alpha(t)x_0 + \alpha(t')x_0}{\beta(t)} \\ &= \frac{1}{\beta(t)}(x_t - x_{t'}) + (\frac{1}{\beta(t)} - \frac{1}{\beta(t')})(x_{t'} - \alpha(t')x_0) + \frac{\alpha(t') - \alpha(t)}{\beta(t)}x_0\end{aligned} \tag{46}$$

Take an upper bound of the norm:

$$\begin{aligned}||\epsilon_\theta(x_t, t, c) - \epsilon_\theta(x_{t'}, t', c)|| \le \frac{1}{\beta(t)}||x_t - x_{t'}|| \\ + ||x_{t'} - \alpha(t')x_0|| \mid \frac{1}{\beta(t)} - \frac{1}{\beta(t')} \mid + ||x_0|| \frac{\mid \alpha(t') - \alpha(t) \mid}{\mid \beta(t) \mid}\end{aligned} \tag{47}$$

Since α and β vary with time t within the interval $[0, 1]$, both α and β are Lipschitz continuous:

$$|\alpha(t) - \alpha(t')| \le K_\alpha |t - t'|, \quad |\frac{1}{\beta(t)} - \frac{1}{\beta(t')}| \le K_\beta |t - t'|. \tag{48}$$

To avoid potential issues with infinite Lipschitz (Yang et al., 2023) constants near the boundaries, we skip the last time steps. Therefore, β has a lower bound that $\beta(t) \geq \beta_{min} > 0$. We can get the formulation below:

$$\begin{aligned} ||\epsilon_\theta(x_t, t, c) - \epsilon(x_{t'}, t', c)|| &\leq \frac{1}{\beta_{min}} ||x_t - x_{t'}|| \\ &+ ||x_{t'} - \alpha(t')x_0|| K_\beta |t - t'| + ||x_0|| \frac{K_\alpha}{\beta_{min}} |t - t'|) \end{aligned} \tag{49}$$

In generation tasks, x_0 is often bounded (e.g., in image generation tasks, pixel values are normalized between 0 and 1), thus we defind $x_0 \leq K_0$. Since $x_t{}'$ lies along the denoising path from x_T to x_0, it follows that $||x_{t'} - f(t')x_0|| \leq ||x_T - x_0||$. Furthermore, since $x_T \sim \mathcal{N}(0, I)$, we also have $||x_T - x_0|| \leq K_1$. We can get the formulation:

$$||\epsilon_\theta(x_t, t, c) - \epsilon_\theta(x_{t'}, t', c)|| \leq L_x ||x_t - x_{t'}|| + L_t ||t - t'||, L_x = \frac{1}{\beta_{min}}, L_t = K_1 K_\beta + \frac{K_0 K\alpha}{\beta_{min}} \tag{50}$$

Therefore, the model output $\epsilon_\theta(x_t, t, c)$ is jointly Lipschitz continuous in both x_t and t, exhibiting structured and predictable variations across time steps.

A.5 Accumulated error when each timestep introduces a fixed error

Assuming that a fixed error β is introduced at every timestep. The accumulated error after a single sampling step can then be expressed as follows:

$$x_{T-1}^{'} = f(T-1) \cdot x_T - g(T-1) \cdot (\epsilon_\theta(x_T, T, c) - \beta) \tag{51}$$

Similarly, we can obtain the following formula after the second sampling using the approximated noise and substituting Equation 11:

$$\begin{aligned} x_{T-2}^{'} &= f(T-2) \cdot x_{T-1}^{'} - g(T-2) \cdot (\epsilon_\theta(x_{T-2}, T-2, c) - \beta) \\ &= f(T-2) \cdot f(T-1) \cdot x_T - f(T-2) \cdot g(T-1) \cdot \epsilon_\theta(x_T, T, c) \\ &+ (f(T-2) \cdot g(T-1) + g(T-2)) \cdot \beta - g(T-2) \cdot \epsilon_\theta(x_{T-1}, T-1, c). \end{aligned} \tag{52}$$

By analogy, we can obtain the following results after sampling T times:

$$\begin{aligned} x_0^{'} &= \prod_{j=0}^{T-1} f(j) \cdot x_T - g(0) \cdot \epsilon_\theta(x_1, 1, c) - \sum_{m=0}^{T-2} \left(\left(\prod_{j=0}^{T-2-m} f(j) \right) \cdot g(T-1-m) \cdot \epsilon_\theta(x_{T-m}, T-m, c) \right) \\ &\underbrace{+ \sum_{m=0}^{T-2} \left(\left(\prod_{j=0}^{T-2-m} f(j) \right) \cdot g(T-1-m) \cdot \beta \right) + g(0) \cdot \beta}_{cumulative\ \ error}. \end{aligned} \tag{53}$$

It can be seen that there is an additional error accumulation term on top of Equation 11 obtained by normal denoising. The error at each step is amplified throughout the sampling process. Therefore, we must ensure that the accumulated error within a single approximation round does not cause the trajectory to deviate; otherwise, the deviation would become even larger after multiple rounds of accumulation.

A.6 Algorithm of consistent trend predictor

Algorithm 1 illustrates the workflow of our consistent trend predictor. The consistent trend predictor is applied during the stable phase of the denoising process, leveraging the smooth continuity of diffusion trajectories, projecting historical de- noising patterns into stable future directions and progressively distributing them across multiple approximation steps to achieve acceleration without deviating.

Algorithm 1 Consistent Trend Predictor.

```
Input: Diffusion Model $\epsilon_\theta$, Sampling Scheduler $\phi$, Decoder $D$, Sample Step $T$, Conditional Embedding $c$,
    Pre-Inference step $n$, Smoothing Factor $\alpha$, Error Threshold $\sigma$;
 1: Initialize Random Noise $x$, Future Trend $\Delta$ = None, Approximation Step $k$ = 0, Previous Model Output
    $P$ =None.
 2: for $t = T$ to $T - n$ do
 3:     if $t = T - 1$ then
 4:         $\Delta = \epsilon_\theta(x, t, c) - P$;
 5:     end if
 6:     if $t < T - 1$ then
 7:         $\Delta = (1 - \alpha)\Delta + \alpha(\epsilon_\theta(x, t, c) - P)$;
 8:     end if
 9:     $P = \epsilon_\theta(x, t, c)$);
10:     Compute $\phi(x, \epsilon_\theta(x, t, c))$ by Eq. (1);
11: end for
12: while $t > 1$ do
13:     for $j = 1$ to $k$ do
14:         $\epsilon_\theta^{'}(x, t - j, c) \leftarrow P + \frac{\Delta}{k}$;
15:         $P = \epsilon_\theta^{'}(x, t - j, c)$);
16:         Compute $\phi(x, \epsilon_\theta^{'}(x, t - j, c))$ by Eq. (1);
17:     end for
18:     $t \leftarrow t - k - 1$;
19:     if $\epsilon_\theta(x, t, c) - P - \Delta \geq \sigma$ then
20:         if $k > 0$ then
21:             $k = k - 1$;
22:         end if
23:     end if
24:     if $\epsilon_\theta(x, t, c) - P - \Delta < \sigma$ then
25:         $k = k + 1$;
26:     end if
27:     $\Delta = (1 - \alpha)\Delta + \alpha(\epsilon_\theta(x, t, c) - P)$;
28:     $P = \epsilon_\theta(x, t, c)$);
29:     Compute $\phi(x, \epsilon_\theta(x, t, c))$ by Eq. (1);
30: end while
31: Compute $\phi(x, \epsilon_\theta(x, t - 1, c))$ by Eq. (1);
32: return $D(x)$.
```

A.7 Algorithm of consistent trend predictor

Algorithm 2 Model-Specific Error Tolerance Search Mechanism.

```
Input: Diffusion Model $\epsilon_\theta$, Sampling Scheduler $\phi$, Decoder $D$, Sample Step $T$, Conditional Embedding Set
    $S_c$, Trend Inflection Point Analysis Model $M$, Similarity Metrics $Sim$;
 1: Initialize Similarity List S=[0]*($T - 1$).
 2: for $c$ in $S_c$ do
 3:     Initialize Random Noise $x$, Previous Output $P$ = None, Model Output Differences List $L$=[];
 4:     for $t = T$ to 0 do
 5:         if $t < T$ then
 6:             $L$.append(($\epsilon_\theta(x, t, c) - P).abs().mean()$);
 7:         end if
 8:         $P = \epsilon_\theta(x, t, c)$;
 9:         Compute $\phi(x, \epsilon_\theta(x, t, c))$ by Eq. (1);
10:     end for
11:     for $i = 0$ to $T - 1$ do
12:         Initialize Random Noise $x^{'}$;
13:         $x^{'} = x^{'}/x^{'}.mean() * L[i]$;
14:         S[$i$] = S[$i$]+$Sim(D(x + x^{'}), D(x))$;
15:     end for
16: end for
17: S = S/($T$-1);
18: $\sigma$ = $M$(S); return $\sigma$
```

Table 5: Quantitative results compared with intra-layer feature reuse methods. Best performance in **bold**, and the second best <u>underlined</u>.

Method	**Visual Quality**				**Efficiency**		
Text to Image	**LPIPS** ↓	**SSIM** ↑	**PSNR** ↑	**CLIP** ↑	**FLOPs (P)** ↓	**Speedup** ↑	**Latency (s)** ↓
SDXL ($T = 50$)	-	-	-	27.253	0.67	1×	9.63
ETC ($\sigma = 0.0171$)	**0.105**	**0.876**	**28.017**	**27.103**	0.26	2.12×	4.53
DeepCache	<u>0.205</u>	<u>0.791</u>	<u>23.871</u>	<u>27.055</u>	<u>0.25</u>	<u>2.17×</u>	<u>4.33</u>
DeepCache+ETC	0.231	0.782	22.547	27.049	**0.14**	**4.29**×	**2.24**
FLUX ($T = 50$)	-	-	-	26.319	3.64	1×	28.85
ETC	**0.068**	**0.926**	**29.176**	**25.983**	1.31	2.65×	10.86
ToCa	<u>0.322</u>	<u>0.694</u>	<u>18.387</u>	25.286	<u>1.86</u>	1.88×	15.31
ToCa+ETC	0.351	0.687	18.187	<u>25.711</u>	**1.01**	**3.43**×	**8.41**
Text to Video	**LPIPS** ↓	**SSIM** ↑	**PSNR** ↑	**VBench** ↑	**FLOPs (P)** ↓	**Speedup** ↑	**Latency (s)** ↓
Open-Sora 1.2 ($T = 30$)	-	-	-	77.18%	3.15	1×	45.29
Ours ($\sigma = 0.2101$)	**0.131**	**0.848**	**24.123**	**76.44%**	<u>1.32</u>	<u>2.15×</u>	<u>21.07</u>
FasterCache	<u>0.166</u>	0.793	23.282	76.37%	2.08	1.58×	28.67
FasterCache+ETC	0.168	<u>0.802</u>	<u>23.389</u>	<u>76.38%</u>	**1.03**	**2.62**×	**17.28**

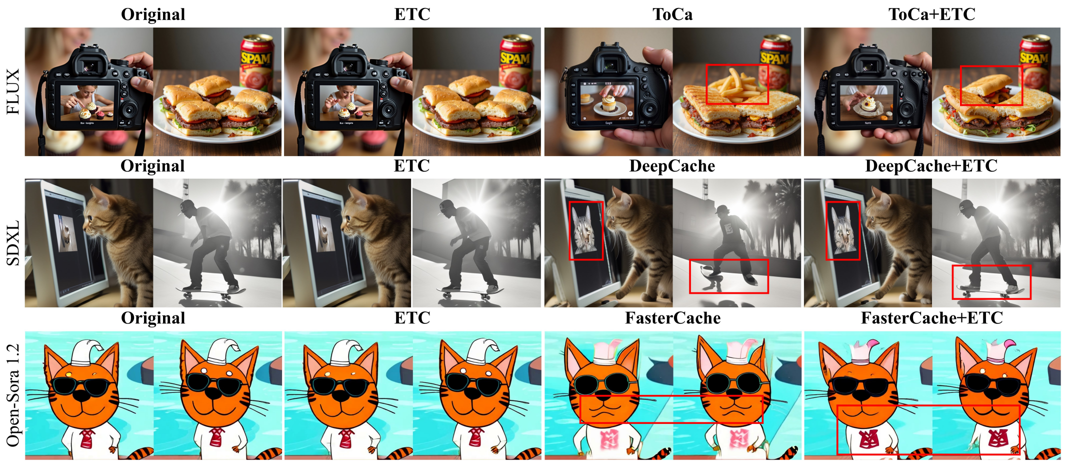

Figure 13: Comparison of visual quality with the intra-layer feature reuse method.

A.8 MORE EXPERIMENTAL RESULTS

A.8.1 COMPARED WITH INTRA-LAYER FEATURE REUSE METHODS

For SDXL, we adopt DeepCache (Ma et al., 2024b), a feature-reuse method designed for U-Net (Ronneberger et al., 2015) that accelerates inference by reusing model features across down-sampling and upsampling blocks. For FLUX, we employ ToCa (Zou et al., 2024), which analyzes token-level importance within DiT (Peebles & Xie, 2023) architectures and reuses low-impact tokens to reduce the computational cost of attention. For Open-Sora, we leverage FasterCache (Lv et al., 2024), a method that accelerates inference by dynamically reusing features within attention modules.For Wan and TangoFlux, although the relevant acceleration techniques are theoretically applicable, no compatible implementations are currently available. Therefore, we do not include experiments for these models. Additionally, our method is compatible with intra-layer feature-reuse approaches, and we include comparative experiments to demonstrate this compatibility.

As shown in Figure 13, our method achieves higher acceleration as well as better generation consistency and quality compared with intra-layer feature–reuse approaches. Furthermore, when combined with intra-layer feature reuse, our method provides additional speedup, while the quality degradation is minimal relative to using intra-layer reuse alone. In some cases, the quality even improves, for example, the structural restoration of a person on a skateboard.

A.8.2 COMPARED WITH TRAINING-BASED FEW STEP MODELS

We also compare our method with trained few-step models. For SDXL, we use SDXL-Lightning (Lin et al., 2024), and for FLUX, we use Flux-Turbo (Alibaba, 2024). Since widely

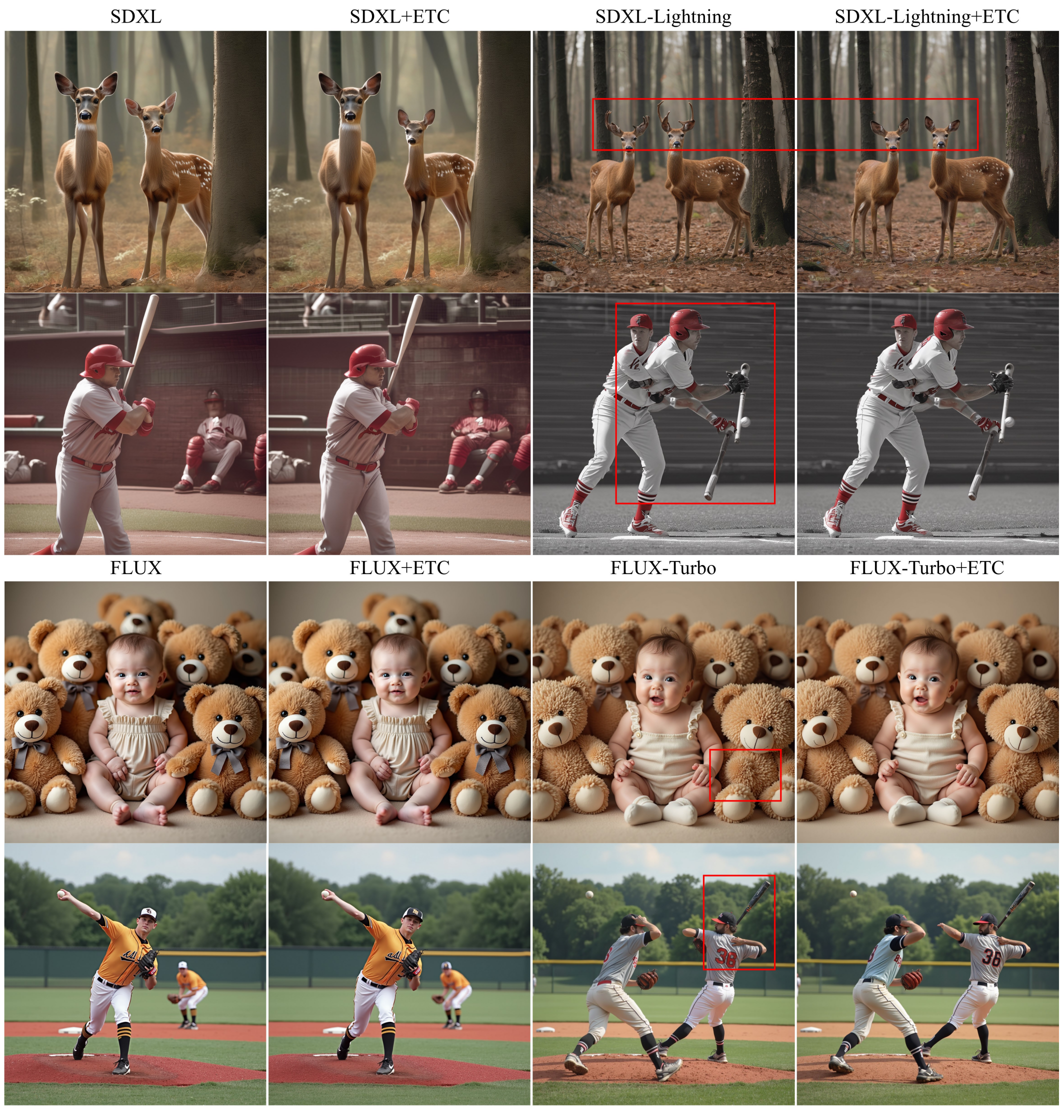

Figure 14: Comparison of visual quality with the trained few-step method.

adopted few-step models for OpenSora, Wan and TangoFlux are not yet publicly available, we omit those experiments for now. In addition, we introduce the MPS (Zhang et al., 2024) metric to evaluate the quality of generated images in terms of attributes such as color, style, and texture.

Table 6: Quantitative results compared with trained few-step methods.

Method	MPS ↑	CLIP ↑	Latency (s) ↓	Speedup ↑
SDXL ($T = 50$)	10.768	**27.253**	9.63	1×
ETC ($T = 50$)	10.701	27.103	4.53	2.12×
SDXL-Lightning ($T = 8$)	**12.003**	26.517	1.41	6.82×
SDXL-Lightning +ETC ($T = 8$)	11.957	26.458	**1.08**	**8.91**×
FLUX ($T = 50$)	**12.941**	**26.319**	28.85	1×
ETC ($T = 50$)	12.898	25.983	10.86	2.65×
FLUX-turbo ($T = 8$)	12.884	25.968	4.87	5.92×
FLUX-turbo +ETC ($T = 8$)	12.852	25.891	**3.42**	**8.43**×

As shown in Table 6, although the trained few-step models achieve substantial improvements in generation speed, they exhibit a noticeable decrease in CLIP scores compared with their multi-step counterparts. While SDXL-Lightning emphasizes aesthetics during training and exceeds the multi-step model on the MPS metric, it also introduces structural distortions—for example, merged human limbs or mixed deer antlers and ears, as illustrated in Figure 14. FLUX-Turbo shows similar issues, such as abnormal hand generation. Moreover, training-based approaches require significant hardware resources. For instance, SDXL-Lightning is trained on 64

Table 7: Quantitative results using different solvers.

Method	Visual Quality				Efficiency		
SDXL	**LPIPS ↓**	**SSIM ↑**	**PSNR ↑**	**CLIP ↑**	**FLOPs (P) ↓**	**Speedup ↑**	**Latency (s) ↓**
DDIM	-	-	-	27.278	0.67	1×	9.27
ETC w/DDIM	0.103	0.881	28.106	27.251	0.27	2.15×	4.31
IPNDM	-	-	-	26.121	0.67	1×	9.31
ETC w/IPNDM	0.119	0.873	27.963	26.063	0.26	2.01×	4.65
DPM++	-	-	-	26.668	0.67	1×	9.15
ETC w/DPM++	0.096	0.882	28.678	26.662	0.24	2.15×	4.26
FLUX	**LPIPS ↓**	**SSIM ↑**	**PSNR ↑**	**CLIP ↑**	**FLOPs (P) ↓**	**Speedup ↑**	**Latency (s) ↓**
Heun	-	-	-	25.522	7.36	1×	50.21
ETC w/Heun	0.053	0.931	29.421	25.301	1.56	4.33×	11.57
UniPC	-	-	-	25.629	3.71	1×	28.54
ETC w/UniPC	0.089	0.912	28.411	25.451	1.12	2.81×	10.13
DPM++	-	-	-	25.734	3.71	1×	28.47
ETC w/DPM++	0.068	0.922	29.052	25.409	1.26	2.78×	10.23
Open-Sora 1.2	**LPIPS ↓**	**SSIM ↑**	**PSNR ↑**	**VBench ↑**	**FLOPs (P) ↓**	**Speedup ↑**	**Latency (s) ↓**
Heun	-	-	-	77.79%	5.96	1×	82.76
ETC w/Heun	0.101	0.874	27.566	77.55%	1.98	2.71×	30.60
UniPC	-	-	-	77.43%	3.08	1×	43.81
ETC w/UniPC	0.125	0.859	25.565	77.06%	1.49	2.08×	21.04
DPM++	-	-	-	77.39%	3.08	1×	43.71
ETC w/DPM++	0.137	0.845	24.114	76.78%	1.09	2.24×	19.43
Wan 2.1	**LPIPS ↓**	**SSIM ↑**	**PSNR ↑**	**VBench ↑**	**FLOPs (P) ↓**	**Speedup ↑**	**Latency (s) ↓**
Heun	-	-	-	81.01%	150.68	1×	1906.29
ETC w/Heun	0.105	0.807	24.155	80.73%	46.29	3.16×	603.26
Euler	-	-	-	81.09%	76.57	1×	966.22
ETC w/Euler	0.079	0.843	25.293	80.88%	29.03	2.43×	396.81
DPM++	-	-	-	81.03%	75.39	1×	958.85
ETC w/DPM++	0.093	0.825	24.867	80.74%	29.16	2.42×	397.11
TangoFlux	**FAD ↓**	**MCD ↓**	**KL ↓**	**CLAP ↑**	**FLOPs (T) ↓**	**Speedup ↑**	**Latency (s) ↓**
Heun	-	-	-	13.285	92.85	1×	10.98
ETC w/Heun	0.027	1.879	0.158	13.273	28.82	2.59×	4.23
UniPC	-	-	-	13.209	46.86	1×	5.56
ETC w/UniPC	0.029	1.885	0.149	13.189	14.83	2.45×	2.27
DPM++	-	-	-	13.276	46.86	1×	5.50
ETC w/DPM++	0.027	1.880	0.153	13.270	14.83	2.43×	2.26

A100 80GB GPUs with a batch size of 512. In contrast, our method is friendly to consumer-level hardware while preserving both generation quality and inference speed. Additionally, our approach can be combined with few-step models to achieve an extra 20%–30% acceleration while maintaining consistent outputs, demonstrating its effectiveness and general applicability.

A.8.3 Acceleration performance across different solvers

Solvers detail All solvers are using the schedulers provided by the Diffusers library[2]. For FLUX, OpenSora, TangoFlux and Wan, where the model output is v, we specify $prediction\_type = flow\_prediction$ when using the scheduler.

Quantitative and qualitative results As shown in Table 7 and Figure 15, our method maintains consistent acceleration and generation quality across different solvers without re-tuning the threshold. This indicates that the threshold we search for captures the error tolerance that prevents trajectory deviation in the model's outputs. Since this property is intrinsic to the model rather than to the choice of solver, the same threshold remains applicable as long as the model itself is unchanged.

A.8.4 Acceleration performance across different resolutions

To further evaluate the robustness of our acceleration method, we evaluate ETC under different resolutions without changing the threshold. For image generation models, we use resolutions of 768×1344 (9:16) and 1152×896 (5:4). For video generation models, OpenSora is tested with 360p

[2]`https://github.com/huggingface/diffusers/`

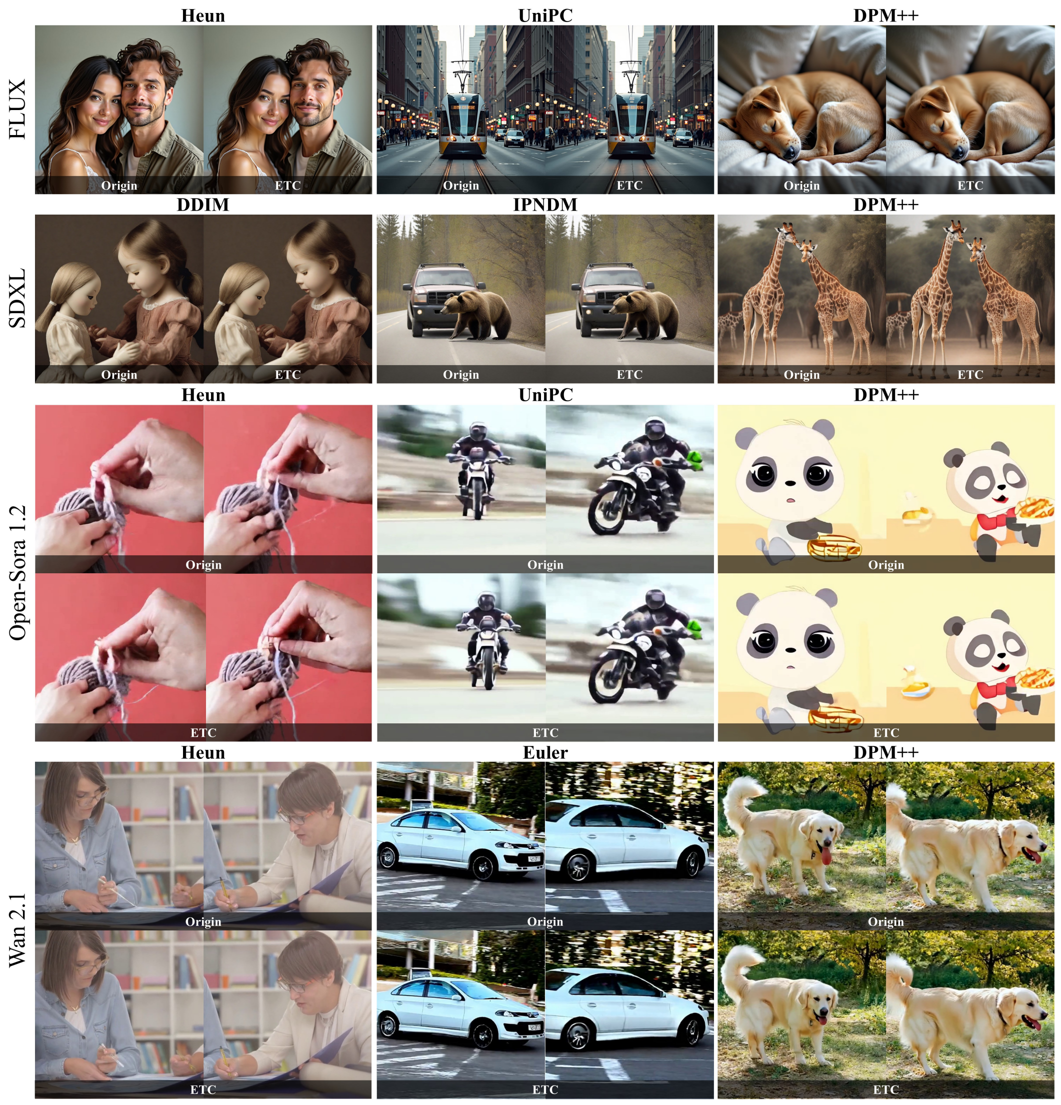

Figure 15: Comparison of visual quality using different solvers.

Table 8: Quantitative results across different resolutions.

Method	Visual Quality				Efficiency		
Text to Image	**LPIPS ↓**	**SSIM ↑**	**PSNR ↑**	**CLIP ↑**	**FLOPs (P) ↓**	**Speedup ↑**	**Latency (s) ↓**
SDXL (768×1344)	-	-	-	27.228	0.67	1×	9.28
ETC	0.114	0.873	27.937	27.045	0.24	2.11×	4.38
SDXL (1152×896)	-	-	-	27.221	0.67	1×	9.31
ETC	0.103	0.879	28.113	27.048	0.23	2.12×	4.37
FLUX (768×1344)	-	-	-	26.429	3.67	1×	28.65
ETC	0.071	0.914	29.093	26.151	1.26	2.69×	10.68
FLUX (1152×896)	-	-	-	26.139	3.67	1×	28.59
ETC	0.069	0.919	29.189	26.058	1.25	2.68×	10.62
Text to Video	**LPIPS ↓**	**SSIM ↑**	**PSNR ↑**	**VBench ↑**	**FLOPs (P) ↓**	**Speedup ↑**	**Latency (s) ↓**
Open-Sora (360p,4:3)	-	-	-	76.89%	1.76	1×	25.86
ETC	0.125	0.868	25.657	76.63%	0.76	2.14×	12.16
Open-Sora (720p,1:1)	-	-	-	77.22%	6.75	1×	105.88
ETC	0.151	0.853	24.624	76.98%	2.02	2.23×	46.52
Wan 2.1 (720×1280)	-	-	-	82.79%	182.95	1×	3456.53
ETC	0.089	0.853	26.763	82.56%	68.83	2.78×	1218.98

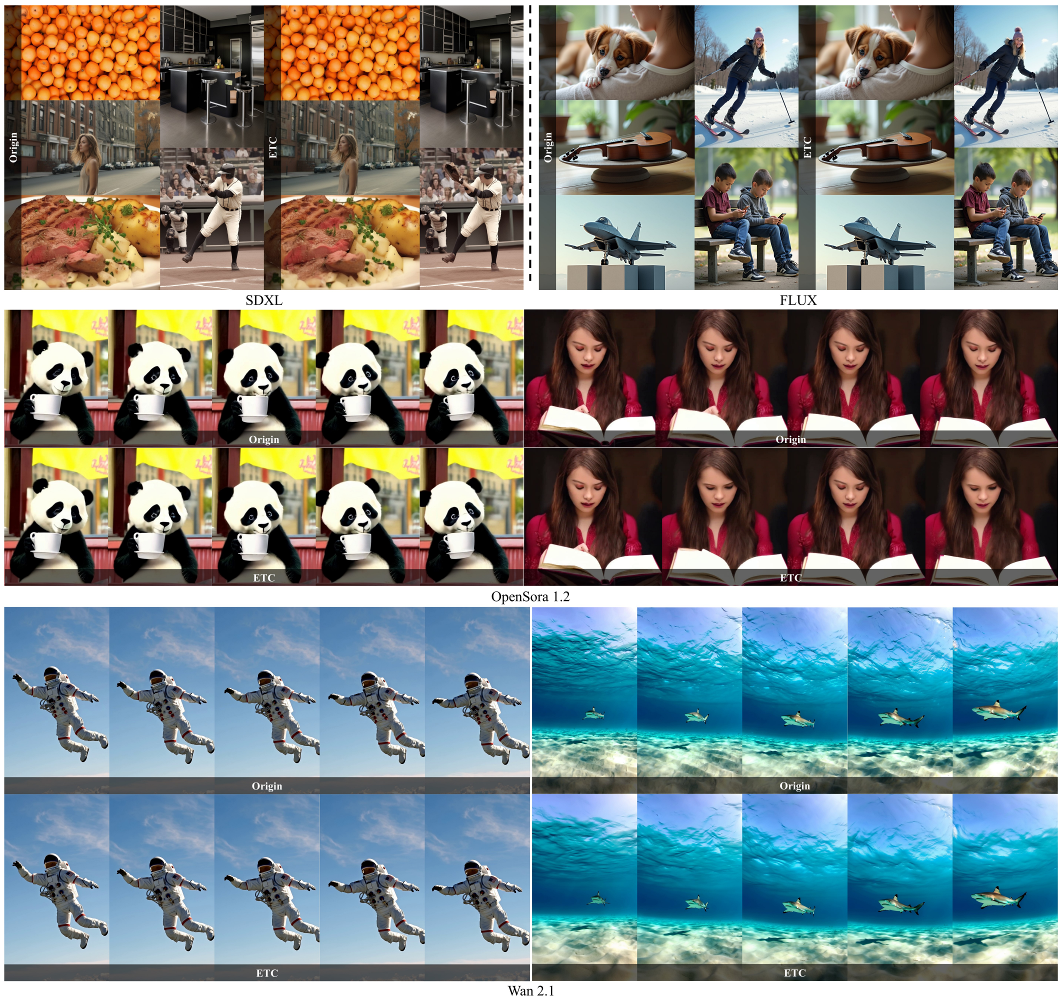

Figure 16: Comparison of visual quality at different resolutions.

Table 9: Quantitative results of dense text generation.

Method	**Visual Quality**				**Efficiency**		
Text to Image	**LPIPS** ↓	**SSIM** ↑	**PSNR** ↑	**CLIP** ↑	**FLOPs (P)** ↓	**Speedup** ↑	**Latency (s)** ↓
SDXL	-	-	-	30.584	0.67	1×	9.82
ETC	0.109	0.865	27.958	30.893	0.28	1.98×	5.08
FLUX	-	-	-	32.547	3.64	1×	29.19
ETC	0.083	0.916	28.344	32.286	1.31	2.51×	11.49

(4:3) and 720p (1:1) settings, while Wan is tested at a resolution of 720×1280. As shown in Table 8 and Figure 16, our method maintains consistent acceleration and stable generation quality across different resolution settings.

A.8.5 Acceleration performance in out-of-distribution prompts

Our threshold search is conducted on a small set of prompts, raising the question of whether the method can maintain consistent generation performance under out-of-distribution prompts—especially in scenarios involving high-density text generation—and whether a smaller threshold is required to ensure final quality. Therefore, we evaluate our method on the TextAtlas5M (Wang et al., 2025) evaluation set. As shown in Table 9 and Figure 17, while our method maintains consistent generation quality, the generation time increases. This is because complex sce-

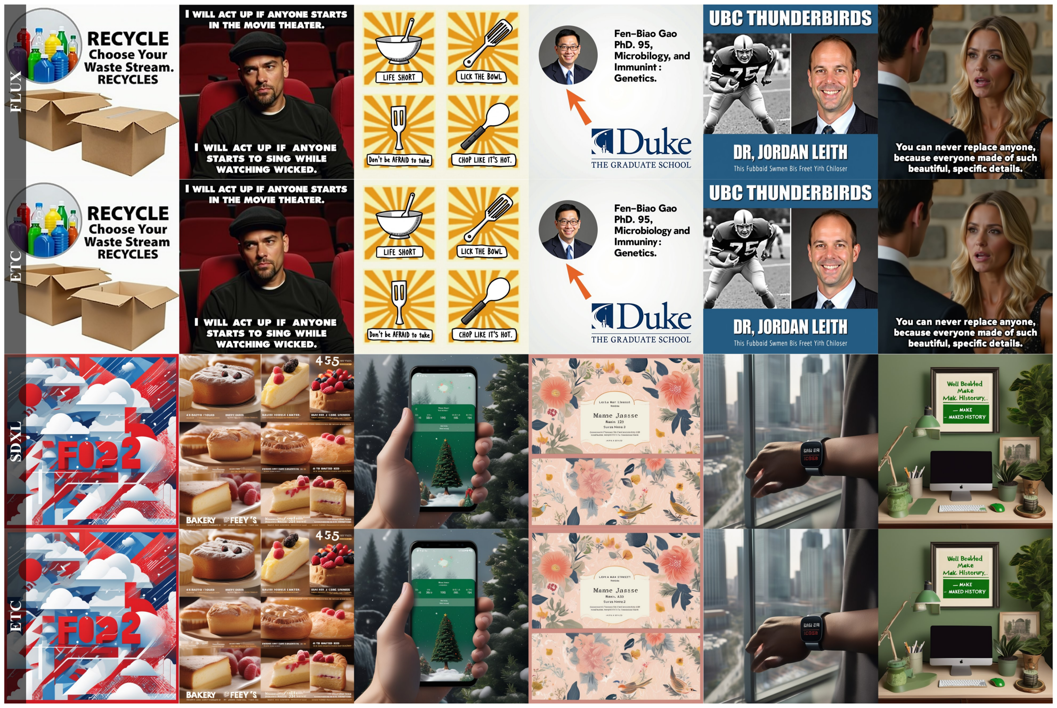
FLUX
ETC
SDXL
ETC
RECYCLE
Choose Your Waste Stream. RECYCLES
I WILL ACT UP IF ANYONE STARTS IN THE MOVIE THEATER.
I WILL ACT UP IF ANYONE STARTS TO SING WHILE WATCHING WICKED.
LIFE SHORT
LICK THE BOWL
Don't be AFRAID to take
CHOP LIKE IT'S HOT.
Fen-Biao Gao PhD. 95, Microbiology, and Immunint : Genetics.
Duke
THE GRADUATE SCHOOL
UBC THUNDERBIRDS
DR. JORDAN LEITH
You can never replace anyone, because everyone made of such beautiful, specific details.
F022
BAKERY FEEY'S
455
Well Beakfed Make Mak Historury.
MAKE HISTORY

Figure 17: Comparison of visual quality at different resolutions.

Table 10: Quantitative results with more aggressive acceleration.

Method	Visual Quality				Efficiency		
Text to Image	LPIPS ↓	SSIM ↑	MPS ↑	CLIP ↑	FLOPs (P) ↓	Speedup ↑	Latency (s) ↓
SDXL	-	-	10.768	27.253	0.67	1×	9.63
ETC	0.105	0.876	10.701	27.103	0.26	2.12×	4.53
ETC-fast	0.336	0.694	10.679	26.898	0.12	4.91×	1.88
FLUX	-	-	12.941	26.319	3.64	1×	28.85
ETC	0.068	0.926	12.898	25.983	1.31	2.65×	10.86
ETC-fast	0.303	0.766	12.871	25.676	0.75	4.63×	6.25
Text to Video	**LPIPS ↓**	**SSIM ↑**	**PSNR ↑**	**VBench ↑**	**FLOPs (P) ↓**	**Speedup ↑**	**Latency (s) ↓**
Open-Sora	-	-	-	77.18%	3.15	1×	45.29
ETC	0.131	0.848	24.123	76.44%	1.32	2.15×	21.07
ETC-fast	0.591	0.492	10.967	76.29%	0.797	4.06×	10.67
Wan 2.1 ($T = 50$)	-	-	-	81.01%	76.71	1×	970.49
ETC	0.103	0.806	24.078	80.71%	28.63	2.49×	389.89
ETC-fast	0.299	0.603	18.193	80.48%	17.58	4.49×	215.67

narios are more prone to trajectory deviation, resulting in more frequent application of the threshold constraint. This indicates that the threshold derived from a small data set maintains robustness.

A.9 More aggressive acceleration

To assess the stability of generation quality under higher acceleration, we apply a larger number of approximation times in the first round of consistent trend predict ($k = 4$). As shown in Table 10, our method achieves a 4–5× speedup. Although consistency drops significantly under this higher acceleration setting, the overall generation quality remains stable—both the CLIP score and the VBench score stay at high levels. Figure 18 presents a good-case example under high acceleration, demonstrating that our method does not suffer from noticeable quality collapse even in this regime, indicating robustness and acceleration potential.

Problems arising from trajectory deviation Although our method maintains a certain level of generation quality under high acceleration, the lack of strict constraints causes deviations in the denoising trajectory, which in turn leads to several issues. In addition to the decreases observed

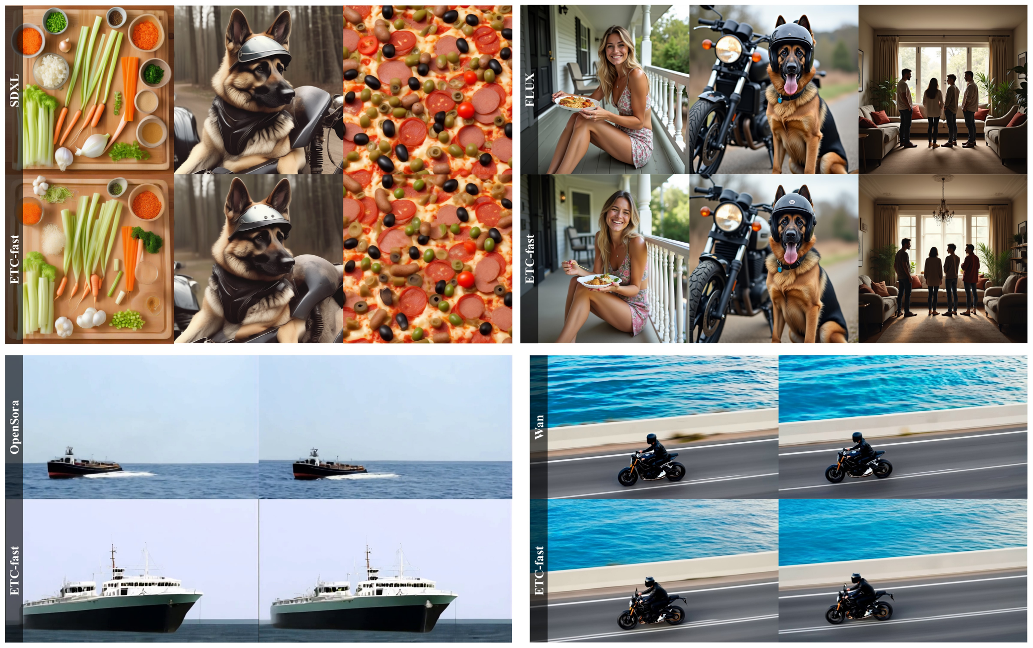

Figure 18: Visual quality under aggressive acceleration.

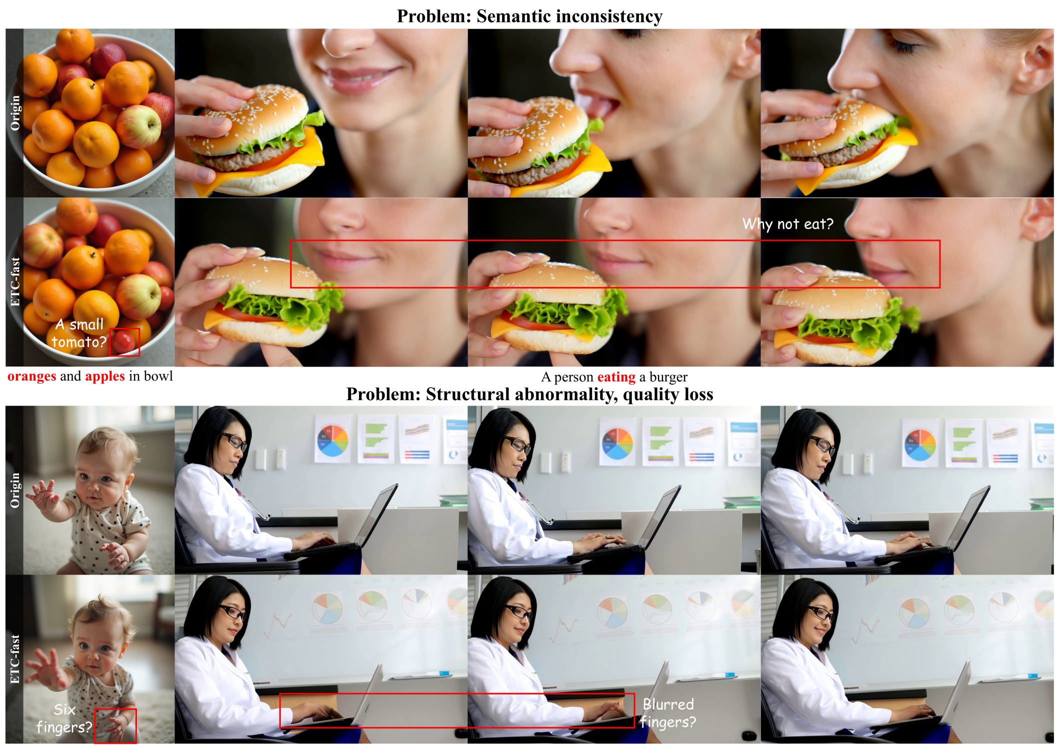

Figure 19: Problems arising from trajectory deviation.

in CLAP, MPS, and VBench metrics in Table 10, we also identify two common problems illustrated in Figure 19. For semantic inconsistency, the generated content does not fully align with the prompt—for example, generating a person with a hamburger but without the intended eating action. For structural abnormalities, highly fine-grained and structured regions such as hands or text often exhibit distortion or deformation. Therefore, our designs for trend consistency and error control aim to minimize deviations from the target generation trajectory and preserve quality under acceleration.

Table 11: Comparison of computational cost between our method and the full-history trend storage approach. Best performance in **bold**.

Method	Visual Quality				Efficiency		
SDXL	**LPIPS ↓**	**SSIM ↑**	**PSNR ↑**	**CLIP ↑**	**FLOPs (M) ↓**	**VRAM (MB) ↓**	**Latency (s) ↓**
ETC	0.105	**0.876**	28.017	27.103	**9.61**	**0.75**	**4.53**
ETC w/all-trend	**0.103**	0.875	**28.025**	**27.105**	35.14	3.44	4.82
FLUX	**LPIPS ↓**	**SSIM ↑**	**PSNR ↑**	**CLIP ↑**	**FLOPs (M) ↓**	**VRAM (MB) ↓**	**Latency (s) ↓**
ETC	**0.068**	**0.926**	29.176	**25.983**	**25.83**	**1.01**	**10.86**
ETC w/all-trend	0.070	0.925	**29.177**	25.976	67.72	6.73	11.35
OpenSora	**LPIPS ↓**	**SSIM ↑**	**PSNR ↑**	**VBench ↑**	**FLOPs (M) ↓**	**VRAM ↓**	**Latency (s) ↓**
ETC	0.131	**0.848**	**24.123**	**76.44%**	**23.65**	**18.34**	**21.07**
ETC w/all-trend	**0.128**	0.848	24.119	76.44%	74.03	39.22	23.51
Wan 2.1	**LPIPS ↓**	**SSIM ↑**	**PSNR ↑**	**VBench ↑**	**FLOPs (M) ↓**	**VRAM ↓**	**Latency (s) ↓**
ETC	**0.103**	**0.806**	24.078	**80.71%**	**211.76**	**40.99**	**389.89**
ETC w/all-trend	0.105	0.805	**24.101**	80.69%	624.79	104.21	397.34
TangoFlux	**FAD ↓**	**MCD ↓**	**KL ↓**	**CLAP ↑**	**FLOPs (M) ↓**	**VRAM ↓**	**Latency (s) ↓**
ETC	**0.026**	**1.877**	0.157	13.251	**4.74**	**0.94**	**2.26**
ETC w/all-trend	0.028	1.877	**0.155**	**13.252**	11.51	3.31	2.53

A.9.1 Computational cost of our method

To evaluate the computational overhead of our method, we measure both VRAM consumption and FLOPs. In addition, to assess the effectiveness of recursively computing trends, we compare our approach with an alternative method that estimates future trends by storing all historical trends. For this baseline, we apply an exponentially increasing weighting scheme in which older trends receive smaller weights and more recent trends receive larger weights, with all weights sum to 1.

As shown in Table 11, our method requires only a few of megabytes of additional VRAM during diffusion inference, and its computational cost is negligible compared with the overall diffusion model inference. This demonstrates that our approach is computation-efficient. Moreover, compared with the method that stores all historical trends to estimate future trends, our recursive formulation achieves comparable acceleration performance and generation quality while reducing both computational cost and memory consumption by more than 50%, thereby significantly mitigating the overhead introduced by trend computation.

A.9.2 A feasible strategy for dynamically adapting α and n

Adaptive n The purpose of setting n is to ensure that our acceleration method is applied only after the diffusion model reaches a stable denoising phase. The threshold σ is obtained by analyzing the transition point between the semantic planning stage and the stable quality-improvement stage of the diffusion process. Therefore, by checking whether the difference between model outputs at adjacent timesteps falls below this threshold, we can determine when to start acceleration and achieve a dynamic n.

Adaptive α For α, when the difference between the model output and the previous approximation is equal to the estimated trend (i.e., their difference is zero), it indicates that the estimated trend perfectly matches the original denoising trajectory. When the difference becomes larger, it suggests that the current α is insufficient and should be updated in the opposite direction. Conversely, when the difference becomes smaller, it indicates that α is being updated in the correct direction and should continue to move along that trajectory. Based on this, we can design an adaptive α update strategy driven by the gradient of the change. Additionally, α can be set as a matrix of the same size as latent, enabling distinct trend updates for each pixel. The pseudocode for adaptive n and α is shown in Algorithm 3.

Table 12 presents the results of applying our method with adaptive n and α. We observe a slight improvement in generation quality after introducing the dynamic strategy. This suggests that although our method is generally insensitive to the choice of α (as shown by Table 4, where $\alpha = 0.5$ already yields well acceleration performance), adapting α to different levels of accumulated error can further enhance generation quality. Our simple adaptive mechanism already provides gains, indicating that future work could build on this direction by more deeply analyzing how model-output

Table 12: Quantitative results by using adaptive n and α. Best performance in **bold**.

Method	Visual Quality				Efficiency		
Text to Image	**LPIPS ↓**	**SSIM ↑**	**PSNR ↑**	**CLIP ↑**	**FLOPs (P) ↓**	**Speedup ↑**	**Latency (s) ↓**
SDXL ($T = 50$)	-	-	-	27.253	0.67	1×	9.63
ETC	0.105	0.876	**28.017**	27.103	0.26	2.12×	4.53
ETC-adaptive	**0.101**	**0.883**	28.009	**27.129**	**0.26**	**2.16**×	**4.44**
FLUX	-	-	-	26.319	3.64	1×	28.85
ETC	0.068	0.926	29.176	25.983	1.31	2.65×	10.86
ETC-adaptive	**0.061**	**0.928**	**29.211**	**25.989**	**1.29**	**2.74**×	**10.51**
Text to Video	**LPIPS ↓**	**SSIM ↑**	**PSNR ↑**	**VBench ↑**	**FLOPs (P) ↓**	**Speedup ↑**	**Latency (s) ↓**
Open-Sora 1.2 ($T = 30$)	-	-	-	77.18%	3.15	1×	45.29
ETC	**0.131**	0.848	24.123	76.44%	1.32	2.15×	21.07
ETC-adaptive	0.132	**0.852**	**24.235**	**76.58%**	**1.32**	**2.15**×	**21.02**
Wan 2.1 ($T = 50$)	-	-	-	81.01%	76.71	1×	970.49
ETC	**0.103**	0.806	24.078	80.71%	28.63	2.49×	389.89
ETC-adaptive	0.104	**0.812**	**24.101**	**80.92%**	**28.54**	**2.50**×	**388.34**
Text to Audio	**FAD ↓**	**MCD ↓**	**KL ↓**	**CLAP ↑**	**FLOPs (T) ↓**	**Speedup ↑**	**Latency (s) ↓**
TangoFlux ($T = 50$)	-	-	-	13.286	46.86	1×	5.49
ETC	0.026	1.877	0.157	13.251	14.83	2.43×	2.26
AdaptiveDiffusion	**0.022**	**1.796**	**0.156**	**13.263**	**14.76**	**2.43**×	**2.25**

Algorithm 3 Adaptive n and α.

```
Input: Diffusion Model $\epsilon_\theta$, Sample Step $T$, Conditional Embedding $c$, Error Threshold $\sigma$;
 1: Future Trend $\Delta =$ None, Previous Model Output $P = 0$, Smoothing matrix $\alpha$, Previous smoothing matrix $\alpha_p$, Previous trend estimation error $E_t$, Start to acceleration $s =$ False.
 2: for $t = T$ to $T - n$ do
 3:     if not $s$ then
 4:         if $\epsilon_\theta(x, t, c) - P < \sigma$ then
 5:             $s =$True;
 6:         end if
 7:         Update $P$ and $\Delta$;
 8:     else
 9:         Acceleration by using consistent trend predictor;
10:         $grad = (abs(\epsilon_\theta(x, t, c) - P - \delta) - E_t)/(\alpha - \alpha_p + 1e^{-8})$;
11:         $\alpha_p = \alpha$;
12:         $E_t = abs(\epsilon_\theta(x, t, c) - P - \delta)$;
13:         $\alpha = \alpha - grad$;
14:         $\alpha$.clamp(0.1,0.9);
15:     end if
16: end for
17: return $D(x)$.
```

deviations under different error accumulations influence future denoising trajectories. Such analysis could guide more principled adjustments of the trend-update magnitude.

A.10 Online threshold search method for unseen models

Our threshold search is performed offline on a small amount of dataset. However, when encountering new data (e.g. different resolutions or prompts with varying complexity), the offline threshold may still have room for improvement. To investigate this, we design an online threshold search method and compare it with the offline approach. Specifically, we randomly sample and combine seven conditions across different samplers, resolutions, and prompts. For each condition, we perform threshold searching and store the resulting value. Whenever a new threshold is obtained, we update the global threshold by taking the average of all collected thresholds, and then evaluate the acceleration performance under this updated threshold.

As shown in Table 13, small adjustments to the threshold do not lead to significant changes in acceleration performance. As more online search results are accumulated, the threshold gradually converges to a universal value, which also lies near the one obtained by our offline method. This

Table 13: Quantitative results by using online search σ.

Model	σ update round	1	2	3	4	5	6	7
SDXL	σ-search	0.0096	0.0149	0.0108	0.0187	0.0193	0.0203	0.0151
	σ-mean	0.0096	0.0122	0.0115	0.0151	0.0172	0.0187	0.0169
	SSIM↑	0.883	0.879	0.880	0.878	0.876	0.874	0.876
	CLIP↑	27.159	27.122	27.129	27.110	27.105	27.103	27.110
	Latency (s) ↓	5.05	4.79	4.82	4.65	4.55	4.31	4.56
FLUX	σ-search	0.0986	0.1284	0.1032	0.1411	0.1314	0.1102	0.1417
	σ-mean	0.0986	0.1135	0.1083	0.1247	0.1281	0.1191	0.1304
	SSIM↑	0.928	0.927	0.927	0.926	0.926	0.926	0.925
	CLIP↑	26.279	26.087	26.281	25.983	25.982	25.983	25.981
	Latency (s) ↓	11.89	11.02	11.78	10.82	10.85	10.83	10.56
OpenSora	σ-search	0.1841	0.2327	0.1747	0.2505	0.1960	0.2171	0.2006
	σ-mean	0.1841	0.2084	0.1915	0.2210	0.2085	0.2128	0.2067
	SSIM↑	0.852	0.848	0.850	0.845	0.848	0.848	0.848
	VBench↑	76.63%	76.44%	76.52%	76.40%	76.44%	76.44%	76.44%
	Latency (s) ↓	22.23	21.09	21.96	20.98	21.10	21.09	21.05
Wan	σ-search	0.0879	0.1139	0.1016	0.1361	0.1289	0.0977	0.1248
	σ-mean	0.0879	0.1009	0.1012	0.1186	0.1237	0.1107	0.1177
	SSIM↑	0.821	0.810	0.810	0.806	0.793	0.806	0.806
	VBench↑	80.72%	80.71%	80.71%	80.71%	80.61%	80.71%	80.71%
	Latency (s) ↓	495.21	403.55	403.67	392.22	382.19	391.02	390.12
TangoFlux	σ-search	0.0595	0.0756	0.0621	0.0641	0.0701	0.0621	0.0658
	σ-mean	0.0595	0.0675	0.0648	0.0644	0.0672	0.0646	0.0652
	KL↓	0.148	0.157	0.155	0.155	0.157	0.155	0.156
	CLAP↑	13.260	13.251	13.252	13.252	13.251	13.252	13.251
	Latency (s) ↓	2.41	2.23	2.32	2.34	2.25	2.33	2.32

indicates that providing an approximate range for the threshold is sufficient. Consequently, the threshold estimated from a small number of prompts exhibits robustness comparable to that of the online approach.

A.11 Workflow of the trend inflection point analysis model

For the analysis of trend inflection point, we use the Bottom-up (Truong et al., 2020) method from the ruptures library[3]. Bottom-up segmentation, denoted BotUp, starts by splitting the original signal in many small sub-signals and sequentially merges them until there remain only K change points. At every step, all potential change points (indexes separating adjacent sub-segments) are ranked by the discrepancy measure d between the segments they separate. Change points with the lowest discrepancy are then deleted, meaning that the segments they separate are merged. A schematic view of the algorithm is displayed on Figure 20 and an implementation is provided in Algorithm 4. Its benefits are its linear computational complexity and conceptual simplicity. For the discrepancy measure function d, we select Least Absolute Deviation (CostL1). Formally, for a signal $\{y_t\}_t$ on an interval I:

$$c(y_I) = \sum_{t \in I} ||y_t - \overline{y}||_1, \tag{54}$$

where $\overline{y}$ is the componentwise median of $\{y_t\}_{t \in I}$.

[3]`https://github.com/deepcharles/ruptures`

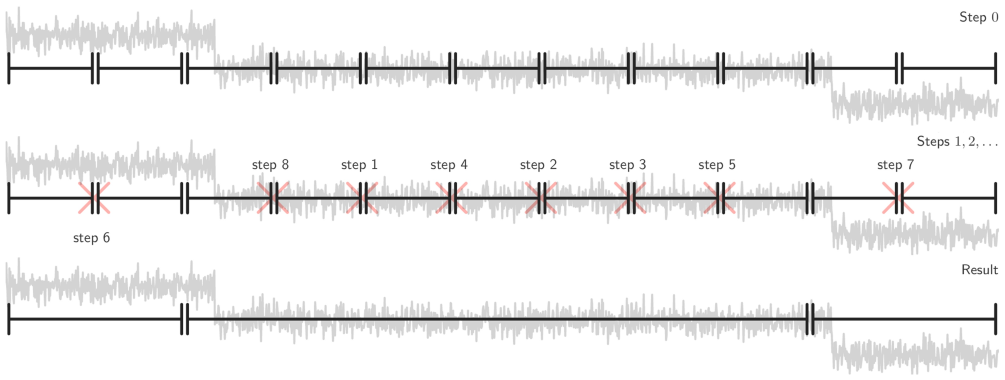

Figure 20: Schematic view of Bottom-up (Truong et al., 2020).

Algorithm 4 Algorithm Bottom-up.

```
Input: signal $\{y_t\}_{t=1}^T$, cost function $c(\cdot)$, stopping criterion, grid size $\delta > 2$.
 1: Initialize $L \leftarrow \delta, 2\delta, \ldots, (\lfloor T/\delta \rfloor - 1)\delta$.
 2: repeat
 3:     $k \leftarrow |L|$.
 4:     $t_0 \leftarrow 0$ and $t_{k+1} \leftarrow T$
 5:     Denote by $t_i (i = 1, \ldots, k)$ the elements (in ascending order) of $L$, ie $L = \{t_1, \ldots, t_k\}$.
 6:     Initialize $G$, a $(k-1)$-long array.
 7:     for $i = 1, \ldots, k-1$ do
 8:         $G[i-1] \leftarrow c(y_{t_{i-1}..t_{i+1}}) - [c(y_{t_{i-1}..t_i)} + c(y_{t_i..t_{i+1}})]$.
 9:     end for
10:     $\hat{i} \leftarrow argmin_i \, G[i]$
11:     Remove $t_{\hat{i}+1}$ from $L$.
12: until stopping criterion is met.
13: return set $L$ of estimated breakpoint indexes.
```

B LLM USAGE

Large Language Models (LLMs) were used to aid in the writing and polishing of the manuscript. Specifically, we used an LLM to assist in refining the language, improving readability, and ensuring clarity in various sections of the paper. The model helped with tasks such as sentence rephrasing, grammar checking, and enhancing the overall flow of the text.

It is important to note that the LLM was not involved in the ideation, research methodology, or experimental design. All research concepts, ideas, and analyses were developed and conducted by the authors. The contributions of the LLM were solely focused on improving the linguistic quality of the paper, with no involvement in the scientific content or data analysis.

The authors take full responsibility for the content of the manuscript, including any text generated or polished by the LLM. We have ensured that the LLM-generated text adheres to ethical guidelines and does not contribute to plagiarism or scientific misconduct.